Characterisation of a Prototype Solar Three-Dimensional Printer

Author: Thomas Simon Böhmer

Supervisor: Heinrich Badenhorst

Co-Supervisor: Paul Walter Sonnendecker

A dissertation in partial fulfilment of the requirements for the degree of Master of Engineering in Chemical Engineering

Department of Chemical Engineering

Faculty of Engineering, Built Environment and IT

University of Pretoria

South Africa

October 2018

Synopsis

Rapid prototyping techniques are quickly advancing to become market leading manufacturing techniques in terms of: product availability, cost effectiveness and environmental impact. In addition, they are also rendering many traditional manufacturing techniques, still employed by small manufacturers or crafters, obsolete. In an attempt to create an even more sustainable rapid prototyping technique, that is cheaper and simpler to construct, the concept of a prototype three-dimensional (3D) printer, that uses concentrated solar power to sinter a salt, which acts as calibrant, has been developed. In order to test and calibrate this prototype, a thermodynamic model was developed to predict thermal properties of mixtures of materials. These, and conventional materials, were subsequently tested on a constructed prototype printer.

The thermodynamic model was found to be able to make reasonably accurate predictions, with average errors of 12 % for the eutectic temperature and 30.6 % for the latent heat of fusion. Based on these results a eutectic mixture of KNO_3 and $NaNO_3$ was selected for testing as this mixture has thermal properties very similar to those of Nylon used in commercial SLS applications. Printing tests were conducted using a mirror utilising two axis control to collimate sunlight and a Fresnel lens to concentrate it. The printing process was analysed and, through application of a dimensional analysis, a basic control philosophy for this process was developed. This control scheme was able to control the sintered depth well, displaying an average error of only 2.4 %.

The current work established basic principles for the process of rapid prototyping using concentrated solar power. The developed methods are able to predict the influence of environmental effects on the process. However, a low resolution due to a large spot size and warping of polymer parts currently limit its applicability. It is recommended that further investigation into these aspects is conducted.

Keywords: three-dimensional printing, thermodynamic model, concentrated solar power

Publications

Badenhorst, H. & Böhmer, T.S. (2018). Enthalpy of fusion prediction for the optimisation of salt based latent heat thermal energy stores. *Journal of Energy Storage, 20,* 459-472

Acknowledgements

Firstly, I would like to thank my parents. Without their countless contributions, efforts and advice over many years even the thought of a master’s would not have been possible. Secondly, to both my supervisor and co-supervisor— your guidance, supervision and willingness to help in challenging circumstances throughout the project is highly appreciated. Lastly, I would like to thank Ezanne for her encouragement when I needed it most.

Contents

List of Figures

List of Tables

List of Abbreviations

2D	Two-Dimensional
3D	Three-Dimensional
3DP	Three-Dimensional Printing
CAD	Computer Assisted Design
CSP	Concentrated Solar Power
DALM	Direct Additive Laser Manufacturing
DNI	Direct Normal Irradiance
FDM	Fused Deposition Modelling
LOM	Laminated Object Manufacturing
RMS	Root Mean Squared
RP	Rapid Prototyping
SLA	Stereolithography
SLM	Selective Laser Melting
SLS	Selective Laser Sintering

Nomenclature

Symbol	**Description**	**Unit**
A	Area	m^2
b	Contact Size Ratio	-
c	Concentration Ratio	-
C_P	Heat Capacity	$J \cdot kg^{-1} \cdot K^{-1}$
d	Diameter	m
E	Energy Density	$J \cdot m^{-2}$
f	Fugacity	$N \cdot m^{-2}$
G	Gibbs Free Energy	$J \cdot mol^{-1}$
h	Convective Heat Transfer Coefficient	$W \cdot m^{-2} \cdot K^{-1}$
H	Enthalpy	$J \cdot mol^{-1}$
k	Thermal Conductivity	$W \cdot m^{-1} \cdot K^{-1}$
l	Length	m
L_P	Photon Mean Free Path	m
L_t	Layer Thickness	m
p	Perimeter	m

Symbol	Description	Unit
P	Power	W
Q	Heat Flow	W
q	Heat Flux	$W \cdot m^{-2}$
R	Universal Gas Constant	$J \cdot mol^{-1} \cdot K^{-1}$
S	Entropy	$J \cdot mol^{-1} \cdot K^{-1}$
s	Thermal Resistance	$K \cdot W^{-1}$
S_s	Scan Spacing	m
T	Temperature	K
t	Time	s
v	Scanning Velocity	$m \cdot s^{-1}$
x	Mole Fraction	-

Greek Symbols

α	Thermal Diffusivity	$m^2 \cdot s^{-1}$
β	Thermal Expansion Coefficient	K^{-1}
γ	Activity Coefficient	-
Γ	Surface Tension	$N \cdot m^{-1}$

Symbol	**Description**	**Unit**
δ	Thermal Layer Size	m
η	Coupling Efficiency	-
λ	Latent Heat of Fusion	$\mathrm{J{\cdot}mol^{-1}}$
ν	Kinematic Viscosity	$\mathrm{m^2{\cdot}s^{-1}}$
π	Dimensionless Number	-
ρ	Density	$\mathrm{kg{\cdot}m^{-3}}$
σ	Stefan Boltzmann Constant	$\mathrm{W{\cdot}m^{-2}{\cdot}K^{-4}}$
T	Scan Delay	s

Sub- and Superscripts

c	Critical
E	Excess
fus	Fusion
g	Gaseous
l	Liquid
m	Mixture
mp	Melting Point

Symbol	Description	Unit
s	Solid	
v	Vapour	
∞	Surroundings	

1. Introduction

Rapid prototyping (RP) techniques are quickly establishing themselves as viable, fast and one of the most cost-effective manufacturing techniques. These methods allow fabrication of complex three-dimensional (3D) parts directly from starting materials, ideally eliminating both waste and the necessity for post-processing (Agarwala, Bourell, Beaman, Marcus, & Barlow, 1995; Tolochko et al., 2003). This highly effective manufacturing process is created due to the increasingly sophisticated nature of the technologies employed as well as the efficient integration of these technologies into different areas of existing manufacturing processes.

The advantages and benefits of rapid prototyping techniques are numerous and constantly increasing. However, because of very high machine costs, the use of machines capable of these technologies is becoming increasingly exclusive. This makes them unavailable for use by most small-scale hobbyists and reduces the ability of small-scale crafters to compete. It is proposed, in an attempt to rectify this, to develop a new rapid prototyping technology that utilises solar energy to sinter a powdered material. The methodical and automated production of parts in such a manner would be a completely novel application in both rapid prototyping and concentrated solar power (CSP). Through the use of solar energy such a technology will have additional benefits such as greater energy savings. This will make a technology, already aimed at sustainable manufacturing, even more sustainable. Additionally, the technology would have a lesser impact on the environment, not to mention benefits in both cost savings and simplicity when compared to current rapid prototyping techniques relying on similar principles. This technology should be simple enough to be used by craftsmen in rural communities in order to reduce the exclusivity of rapid prototyping technologies.

Because of the requirements of simplicity and low costs, the project is not without foreseeable issues. Conventional laser sintering of metals is done under an inert atmosphere while laser sintering of polymers utilises either an advanced control system to preheat the polymer precursor or a heated bed in order to prevent warping of the final part. Both of these cases are problematic to reconcile with the necessary simplicity, required ease of manufacturing and limited budget of the proposed printer. To overcome these issues, it is proposed to use a combination of salts with thermal properties— such as melting temperature and latent heat of fusion— similar to those of commercial laser sintering powders. By using salts as a model component, which do not oxidise nor warp significantly upon cooling, the abovementioned issues can be negated. Furthermore, by adjusting the mass fractions of the salt combinations, the properties of the mixture can be easily manipulated, allowing for quick variations in between tests. Using combinations of different salts, a variety of properties, ranging from those similar to polymers to properties alike to metals used in SLS, can be obtained. South Africa is an ideal location to develop and utilize such a technology, as the average incident solar radiation is comparatively high throughout the year, with certain parts receiving 2800 $\text{kW}\cdot\text{h}\cdot\text{m}^{-2}$ – 3000 $\text{kW}\cdot\text{h}\cdot\text{m}^{-2}$ annually (Craig, Brent, & Dinter, 2017). Spain, a country investing heavily in CSP, has an average of 2100 $\text{kW}\cdot\text{h}\cdot\text{m}^{-2}$ (Craig et al., 2017).

Because of this solution to the expected problem it is, at first, necessary to develop a thermodynamic model that is able to accurately predict the thermal properties of salt mixtures based only on pure-component data. An additional benefit would be for the model to require as few input properties as possible and for these to be readily available in literature. Following this, a working prototype printer is to be constructed using low-cost and readily available materials to make the overall project as cost efficient and simple to construct as possible. Because a solar tracker, capable of collimating sunlight onto a lens is already available, the investigation need not consider the construction or optimisation thereof. However, because of the natural fluctuations in incoming solar radiation, not to mention other disturbances such as cloud cover and other diverse ambient conditions that the printer will unavoidably be exposed to, the design of a robust control scheme based on successfully validated model equations will be a necessity. The investigation is constrained to the design and characterisation of the printer itself, rather than the code responsible for the manufacture of products from computer assisted design (CAD) files. Numerous versions of these codes are readily available that should be repurposable without too much effort. The study is further limited to polymers and materials with similar characteristics to polymers.

These are materials with a comparatively low temperature and enthalpy of fusion, simplifying the tests without compromising the implications of the results. Although metals are widely utilised in sintering applications, these are not to be investigated in the current study. A large concern is also the ease of manufacturing such a device. As this is aimed at small scale usage as opposed to large industrial application, the printer should be as simple and low cost as possible while adequately fulfilling its purpose.

The objectives of this project are therefore: to develop and validate a thermodynamic model to predict the thermal properties of material mixtures. This model should at least be accurate enough to provide a reasonable first guess. The accuracy of the guess here is subject to the number of components that are to be evaluated. The accuracy should be adjusted to limit the number of systems proposed by the model to one easily evaluable by hand. The precise properties can then be determined, either through analytical methods or from literature. Next, candidate materials with suitable properties should be identified for testing. The design and construction of a running prototype printer, capable of sintering materials using only solar radiation, is the next objective. This printer is then to be used on a material with known and easily adjustable properties with the results used to calibrate the machine. If these tests are successful the printer can be used on materials commonly used in the sintering process, such as polymers. These tests should serve the purpose of relating measurable or manipulated input variables, such as the incident radiation, ambient conditions, material properties or scanning strategies to output variables, such as the sintered depth. Using these results, a suitable control philosophy for the process can be developed.

2. Literature Study

2.1. Current Rapid Prototyping Techniques

Rapid prototyping techniques form part of the so-called additive manufacturing techniques. Additive manufacturing techniques rely on joining materials (Prince, 2014). This is in stark contrast to current, conventional manufacturing techniques which can be labelled as ‘subtractive’. Subtractive methods rely on removing materials from the bulk to create the final product (Prince, 2014). Examples of this are cutting, milling, drilling and other machining processes. Additive manufacturing techniques have several advantages over conventional methods. For instance: only as much material as is needed is used, with leftover materials often in reusable condition, making additive techniques essentially waste free. Waste is also reduced by being allowing increased control over the design of the internal structure, allowing the optimisation of strength and material usage. This makes them cheaper, faster and reduces their environmental impact (Prince, 2014). Additionally, rapid prototyping techniques do not require cutting fluids, the main source of hazardous waste according to Huang *et al.* (2013), another positive factor for environmental impact. A study on the environmental impacts of Direct Additive Laser Manufacturing (DALM) found that environmental impacts are reduced by up to 71 % when compared to conventional methods (Huang et al., 2013). The time it takes to produce a part can also be reduced while the time it takes to implement a part is drastically reduced by allowing for the part to be produced close to or even at the location at which it is to be implemented. This increases the efficiency of the entire supply chain according to Huang *et al.* (2013). Additive techniques also offer the ability to integrate the product planning and testing phases (Levy, Schindel, & Kruth, 2003), allowing for quick, iterative design procedures. These factors are what make additive techniques so attractive to the modern industry.

A variety of rapid prototyping techniques have already been established, such as: Stereolithography (SLA), Fused Deposition Modelling (FDM), Laminated Object

Manufacturing (LOM), Three-Dimensional Printing (3DP), Selective Laser Sintering (SLS) and Selective Laser Melting (SLM).

In SLA— one of the earliest rapid prototyping techniques, already researched upon in the 1970s but patented by Charles Hull in 1986— a photosensitive polymer resin is stored in a transparent vat. Photopolymerisation is induced by scanning over the resin using an ultraviolet laser. The 3D part is essentially drawn in layers in the vat. Once complete, the remaining resin can be poured off to be used in later printing jobs (Prince, 2014). This process is still used today due to its high accuracy.

In FDM, a printing-head melts and extrudes a melted thermoplastic in layers, fusing current layers to previous ones to create a final 3D model (Prince, 2014). It is important that the polymer is heated to only slightly above its melting point so that it solidifies almost instantaneously after being deposited onto the heated bed (Huang et al., 2013). The bed is maintained at a temperature that prevents warping of the produced part. This is the method most commonly employed by hobbyists due to the low cost of both the materials used and of the printer itself.

LOM is performed by stacking sheets of material and bonding them adhesively. A laser is then used to cut away edges to develop the final 3D part. The laser velocity and focus are adjusted so that underlying layers are not damaged. LOM is one of the very few additive processes in which waste is created (Prince, 2014). It should therefore rather be viewed as semi-additive: while material is stacked, this only eliminates waste in one dimension— the axial dimension if viewed in a polar coordinate system. The laser is then used to cut away material in the rotational and angular dimensions.

The principle behind 3DP is that powder layers are deposited on a bed. A printer head, similar to that of an ink-jet printer, then deposits a binding agent on to the powder to solidify certain regions of the layer (Childs, Berzins, Ryder, & Tontowi, 1999).

SLS is one of the industry leading rapid fabrication processes (Simchi, 2006). Developed at the University of Texas in the mid-1980s, it is a technique in which parts are sintered from a powder precursor (Zeng, Pal, & Stucker, 2012). Layers of powder are successively deposited on a lowerable piston and sintered using a laser beam. Support for the sintered part is provided by the remaining unsintered powder bed. This allows for the fabrication of complex 3D parts (A. V. Gusarov, Laoui, Froyen, & Titov, 2003). One method of distinguishing different variants of SLS is between direct SLS and indirect SLS. In indirect SLS a polymer phase is distributed throughout the metal phase as a binder and binds the metal particles upon solidification. Viscous flow and surface energy reduction are the driving forces for the mass flow dissipation in this case (Simchi, 2006). In direct SLS liquid phase sintering, solid state sintering, as well as melting and solidification are the mechanisms responsible for binding the particles. A similar distinction can be made between single component SLS and multicomponent SLS. Single component SLS relies on individual particles being sintered together, as is the case with direct SLS; however, in multicomponent SLS, usually only the component with the lower melting temperature undergoes a phase change, with the component with the higher melting temperature only flowing with the fluid flow (Zeng et al., 2012). This is very similar to the binder being used to solidify solid particles in indirect SLS. SLM is a technique similar to SLS except that the entire product precursor material is melted instead of being sintered, this allows for an increase in density of the final part, while sacrificing accuracy.

2.2. SLS Process

The principle, in general, is that a 3D CAD model, previously designed, is converted or ‘sliced’ into digital layers. Each digital layer is then converted to a physical layer through the sintering of powder and bonded to the preceding layers (Dong, Makradi, Ahzi, & Remond, 2009). This process can also include an optimisation step to optimise the position of multiple components in order to decrease energy consumption, construction time or material usage.

The process set-up for SLS can be described as follows: a powder—either consisting of only one material or of multiple compounds— is spread out evenly over a lowerable piston. This is usually automated and actuated by a roller. At a certain time, t = 0, a constant heat flux source— usually generated by a laser— is applied to a finite region of the assumed semi-infinite powder bed, scanning over the bed systematically. This is usually achieved by manipulating the beam through use of mirrors. Adjacent scanning vectors are located a certain distance apart. This distance is known as the hatch spacing. Heat is transferred into the bed both due to conduction between particles and radiation being reflected between particles, causing it to be channelled into the bed (Bugeda, Cervera, & Lombera, 1999). This is labelled as the first step of SLS by Zhang and Faghri (1999). After a finite duration, during which heat is stored as sensible energy, causing the temperature of the bed to increase, sintering or melting is induced. This is the second step of SLS (Zhang & Faghri, 1999). During this phase the bed is compacted and the surface of the bed lowers. This phase is completed relatively quickly as the particles of the bed are still in equilibrium between the liquid phase and solid phase and the scanning velocity is assumed large relative to the spot size. It is therefore proposed by Zhang and Faghri (1999) that liquid flow effects can be assumed negligible. Once the correct areas of the powder bed have been sufficiently sintered, a new layer of powder is deposited onto the bed and is spread out using the roller until a prescribed layer thickness has been achieved. The same procedure is then followed to sinter the next layer. A schematic of this process for the sintering of a single part can be seen in Figure 2.1, below.

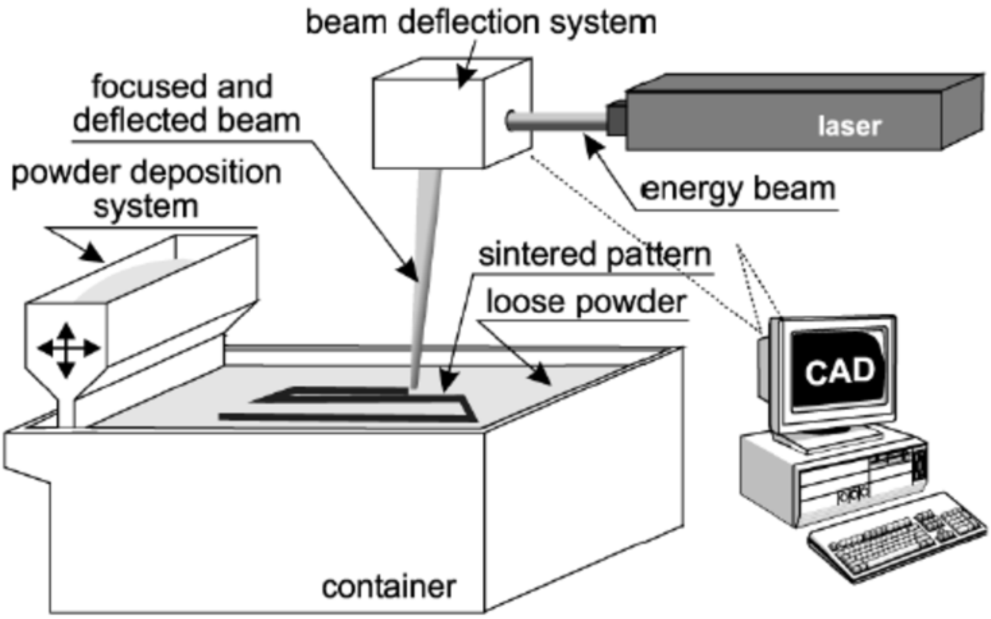

Figure 2.1: Schematic of the SLS Process (Kruth et al., 2003)

Sintering can take place via two different mechanisms. Either through solid state sintering or through liquid phase sintering. Solid state sintering refers to the effect by which necks form between particles and subsequently grow. This is due to the diffusion of individual atoms across particles and grain boundaries (Agarwala et al., 1995). Because the heating duration is so short this is insufficient to cause complete compaction of the product (A. V. Gusarov et al., 2003) and a porous microstructure remains. This is the mechanism by which single component beds are sintered.

Liquid phase sintering is the mechanism by which multicomponent beds, in which the melting temperatures of the individual compounds are significantly different, are sintered. Here, only the particles of the component with the lower melting temperature undergo a phase transition. The liquid phase forms between solid particles which then move with the fluid flow. Liquid phase sintering occurs in three distinct steps (Wang et al., 2002) . In the first step, known as the rearrangement step, the solid particles are rearranged due to the capillary forces acting on them by the liquid phase (Agarwala et al., 1995). In the second step solution precipitation occurs. Finally, the bed is further compacted via solid state sintering. It is, however, the first step that is primarily responsible for liquid phase sintering (Wang et al., 2002).

The process depends on both fabrication and powder parameters (Simchi, 2006). Of the powder characteristics, particle size (Bertrand et al., 2007), and absorptivity (Yap et al., 2015), are the most important. The particle size should be at most one tenth of the layer thickness. A smaller particle size, as well as a greater absorptivity allow for more energy to be imparted into the surface of the bed, causing higher skin temperatures. The geometric shape is also an important factor, with spherical particles exhibiting a better spreadability (Bertrand et al., 2007).

Of the fabrication parameters power, spot size and hatch spacing are noted as the most significant parameters (Simchi, 2006; Williams & Deckard, 1998), with Williams and Deckard adding the scan line length and Simchi adding the scanning strategy; however, these are very similar, as both attempt to quantify the effect of the delay period on the final product. The delay period, τ, is defined as:

$$\tau = \frac{l}{v} \tag{2.1}$$

Higher delay leads to large temperature fluctuations with Simchi (2006) attributing this to greater residual thermal stresses. Zeng, Pal and Stucker (2012) state that a more homogeneous temperature field— which can be created by having a shorter delay period—leads to a better microstructure, mechanical properties and surface finish.

2.3. Problems in Sintering-based Additive Techniques

One of the biggest problems in single component sintering is the phenomenon known as balling. This term is used to describe the formation of small liquid droplets on the surface of the powder layer during sintering. It has a degrading effect on the structure of the powder bed due to surface tension effects. It also adversely affects all following layers due to the displacement of solid particles (Tolochko et al., 2003), decreasing the ability of the following layer to bind to the previous layer correctly. The cause of balling is insufficient wetting with the previous layer during sintering. This is intensified in the sintering of metals as, while in the liquid phase, an oxide layer can form around the droplet, decreasing its wettability (Yap et al., 2015). While in multicomponent sintering balling is not a major issue, in single component sintering techniques the process parameters must be strictly controlled to prevent it (Tolochko et al., 2003). To avoid this phenomenon, it is necessary that the liquid phase adequately wets the previously sintered solid phase (Agarwala et al., 1995). The contact angle, θ, is given by:

$$\cos\theta = \frac{\Gamma_{sv} - \Gamma_{sl}}{\Gamma_{lv}} \tag{2.2}$$

Only limited wetting can occur if the contact angle is greater than 90˚. It must therefore be ensured that the surface tension between liquid phase and the solid phase is lower than that of the solid phase and the vapour phase (Agarwala et al., 1995).

Incomplete densification, leading to a porous final product, is another issue in sintering based additive techniques. Complete compaction is almost never achieved in sintering processes, making post-processing a necessity in cases where a completely dense product is required. A porous final product can be the result of suboptimal processing parameters. A too large hatch spacing or layers that are too thick can cause this problem (Zeng et al., 2012). The hatch spacing must be chosen— based on the power, spot size and scanning velocity of the source— to impart the correct volumetric energy input into the bed. The layer thickness should be chosen to grant maximum accuracy and achieve minimal porosity, whilst not being so thin that the roller displaces previously sintered layers (Agarwala et al., 1995).

High thermal fluctuations, which cause residual stresses, are another possible issue. These can lead to crack formation and possible delamination of layers (Yap et al., 2015). This problem is especially prevalent in ceramics which have a high melting temperature and low thermal conductivity, leading to concentrated high temperature regions. Post processing methods, such as annealing, are required if this becomes a problem. A solution to this problem is to pulse the source at a higher intensity (Fischer et al., 2004). This leads to a higher skin temperature whilst keeping the average temperature of the bed lower. In doing so the melting and resulting consolidation only takes place in the surface layer of each individual grain. According to Fischer *et al.* (2004), this layer should be approximately one tenth of the grain diameter. By using this method, the particles are never completely melted, leading to less shrinkage, higher precision and consequently less residual stress.

Another problem, apparent in all rapid prototyping techniques, is inaccuracy. Conventional manufacturing techniques, such as machining, are still significantly more accurate. Inaccuracies in rapid prototyping techniques have three possible origins (Childs et al., 1999). Firstly, they can arise due to the inaccurate conversion of the CAD model to slice data, describing the individual layer. Machine control errors can also be the cause of inaccuracies. Finally, processing errors can lead to inaccurate production. This can either be due to an offset in the printing procedure or due to residual stresses causing the part to warp during cooling.

Oxidation during the sintering process is a problem when metals are used as the precursor material. The high temperatures during the sintering process cause rapid material degradation if in the presence of oxygen. This can be negated if the process is carried out under an inert atmosphere, such as nitrogen.

2.4. Solar Concentration

The Solar Constant is the amount of extra-terrestrial radiation received outside of the earth's atmosphere— approximately 1366 W·m^{-2}. Radiation across the world is shown in Figure 2.2.

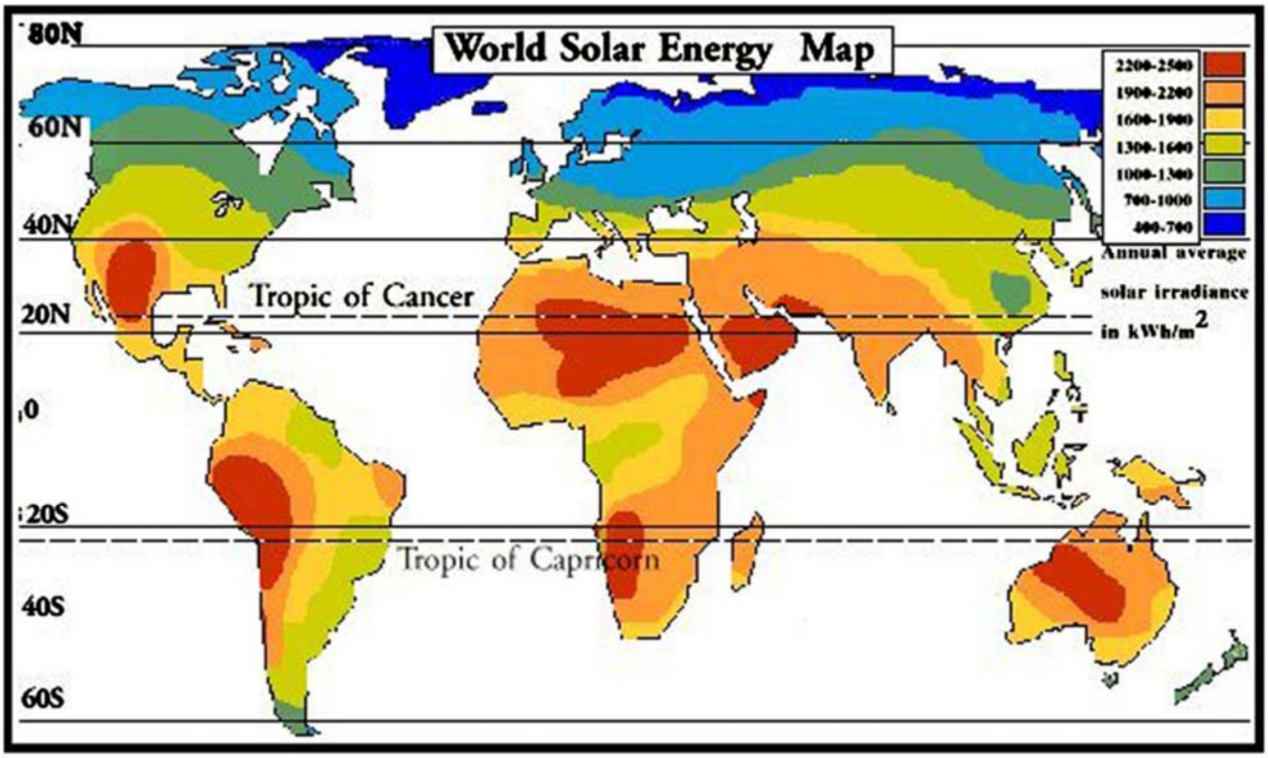

Figure 2.2: World Solar Energy Map (Zhang et al., 2013)

Although the maximum that can be collected on the earth's surface is only approximately 1000 W·m^{-2}, this is still high enough to find application in the surface modification of metals (Sierra & Vazquez, 2005).

The available radiation is, however, hardly exploited and still allows for significant room for improvement. A study conducted by Fluri (2009) with the objective of finding areas suitable for CSP in South Africa also provides valuable information.

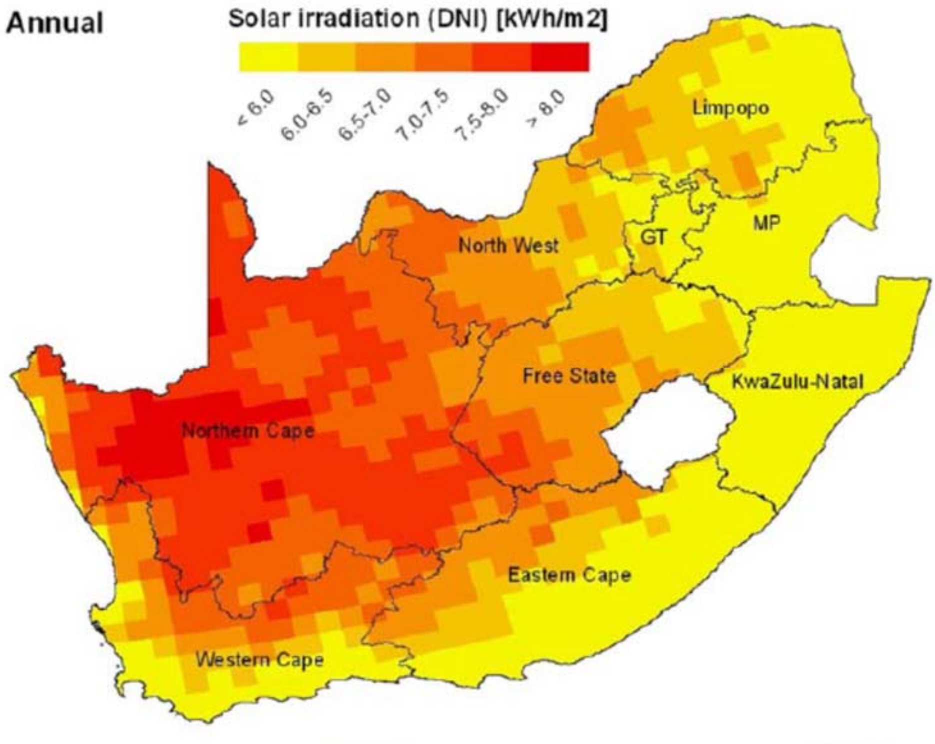

Figure 2.3: Average Annual Direct Normal Irradiations (DNI) in South Africa (Fluri, 2009)

Clearly South Africa— especially the Northern Cape— receives a large amount of solar radiation and is therefore an ideal candidate for the development and implementation of solar energy technologies.

Fresnel lenses offer a cheap, portable and lightweight method of concentrating this energy to utilisable levels. This type of lens, named after its developer, Augustin-Jean Fresnel, reduces a conventional, optical lens to a flat surface. The curvature of the conventional lens is replaced by a repetition of concentric, annular sections with the same curvature. Material which merely transmits radiation without concentrating it is, in this manner, removed, decreasing the weight of the lens. However, due to the discontinuities between annular sections, the concentrating efficiency of Fresnel lenses are always lower than those of their optical counterparts. A schematic of a Fresnel lens, compared to a standard optical lens, is displayed in Figure 2.4.

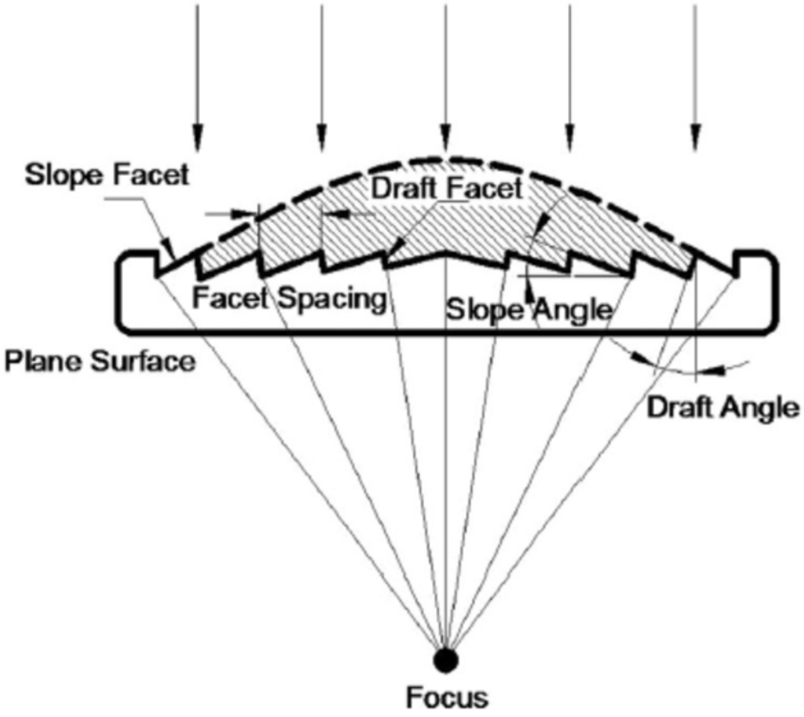

Figure 2.4: Schematic of a Fresnel Lens (Kumar, Shrivastava & Untawale, 2015)

In SLS applications, a concentrated beam of radiation is created through use of a laser. Fresnel lenses can be used replace the laser even though they concentrate radiation in a completely different manner. Although lasers can function on low currents, through implementation of a Fresnel lens this part of the process can be made completely sustainable. While the intensity of a laser source is usually described as a Gaussian relationship with regards to distance from the centre of the beam (Zeng et al., 2012), the ideal intensity of a lens is uniform across the focal point. However, because of the inability to create an ideal lens, it is expected that, through defects, the intensity of a radiation concentrated by a Fresnel lens will have a similar distribution.

A laser has the advantage that the entire generated radiation is at a single wavelength. CO_2 and Nd:YAG lasers— commonly used in these applications—generate radiation at 10.6 μm and 1.06 μm. In contrast, the spectral irradiance of the sun is distributed over a range from 500 nm and 2000 nm. This difference is important to consider when comparing the material's absorption characteristics. Absorption to the radiation produced by these lasers vary drastically: from 23 % to 79 % in metals and 5 % to 94 % in polymers (Kruth et al., 2003). It should therefore come as no surprise if a low efficiency is observed.

Two types of Fresnel lenses are available for this purpose: imaging Fresnel lenses and non-imaging Fresnel lenses. Imaging Fresnel lenses— which are generally not ideal (Leutz and Suzuki, 2012: 8)— are designed to refract light, collected from an object, and create a picture in the focal plane (Xie et al., 2011). They are created to have high concentration ratios, to create a 'sharp' image, but often suffer from manufacturing defects. Non-imaging Fresnel lenses— which can be ideal— are of a lower quality but are cheap and have a flexible design (Xie et al., 2011). Unlike imaging Fresnel lenses, they are not designed to create a sharp image, but rather to collect as much radiation as possible and concentrate this to a high density (Leutz and Suzuki, 2012: 8). Here, ideal refers to the ability of the concentrator to equal the suns brightness and reach its temperature of 5777 K at steady state (Leutz and Suzuki, 2012: 8).

Concentrators can further be categorized as either two-dimensional, or three-dimensional. Two-dimensional concentrators, such as parabolic troughs or linear Fresnel mirror arrays, focus radiation onto a line, whereas three-dimensional concentrators, such as power towers or Stirling dishes, focus energy on a point. Fresnel lenses can be categorised in the same manner. Two-dimensional Fresnel lenses consist of a set of parallel concentrating sections, whereas three dimensional lenses consist of concentric annuli. Naturally, three-dimensional concentrators can concentrate radiation to significantly higher levels and have a significantly higher accuracy. They are therefore much preferred in these types of applications.

The geometric concentration ratio of a Fresnel lens is defined as (Leutz and Suzuki, 2012: 16):

$$c = \frac{A_{aperture}}{A_{absorber}} \tag{2.3}$$

This assumes that no losses occur, which is never truly the case. An efficiency factor should therefore be included. Once the efficiency has been accounted for the concentration ratio is now known as the optical concentration ratio (Leutz and Suzuki, 2012: 16).

The radiation emitted by the sun, incident on the first aperture of the Fresnel lens, can be approximately expressed as (Leutz and Suzuki, 2012: 19):

$$Q = \sigma A_{aperture} \sin^2(0.275°)\, {T_{sun}}^4 \tag{2.4}$$

Where 0.0275˚ is the half-angle of the sun (Leutz and Suzuki, 2012: 19). If the concentrator is ideal its temperature will be equal to that of the sun. The radiation it emits can be approximated by the formula (Leutz and Suzuki, 2012: 19):

$$Q = \sigma A_{absorber} {T_{sun}}^4 \tag{2.5}$$

Equation 2.4 and Equation 2.5 can be equated and rearranged to yield (Leutz and Suzuki, 2012: 19):

$$c_{max} = \frac{A_{aperture}}{A_{absorber}} = \sin^{-2}(0.275) \approx 43400 \tag{2.6}$$

The maximum concentration ratio achievable is therefore approximately 43400. The true temperature of the absorber, assuming ideal efficiency, can therefore be calculated using (Leutz and Suzuki, 2012: 20):

$$T_{absorber} = T_{sun} \sqrt[4]{\frac{c}{c_{max}}} \tag{2.7}$$

A Fresnel lens using a simple, low cost tracking device to collimate light onto it— like the one proposed to be used— has exhibited concentration ratios in excess of 1000 (Badenhorst, Fox, & Mutalib, 2016). Assuming ideal absorption properties, a steady-state temperature of 2250 K can be calculated from Equation 2.6. However, it is expected that even higher values are achievable if a lens specific to the proposed operation is used. Sierra and Vazquez (2005) have noted a heat flux of 260 W·cm^{-2} and surface temperature of approximately 1500 K for a Fresnel lens with a spot size of 5 mm. This is significantly lower than the 10^{3} W·cm^{-2} to 10^{9} W·cm^{-2} achievable with a laser; however, operating with a lens capable of producing a smaller spot size will markedly increase the heat flux and surface temperature.

2.5. Conclusion of Literature

In conclusion a rapid prototyping method using concentrated solar power to directly sinter materials is in many ways very similar to already established methods. The physical process shows many parallels: a CAD model is 'sliced' into digital layers. This data is then transferred to a system which creates an optimal scanning strategy. The digital layers are then converted to physical layers by sintering with a radiative energy source using the proposed scanning strategy. Many of the physical models, developed for SLS or SLM will therefore find application here. Along with this, many of the hurdles in the way of successful laser sintering will be present in the proposed method. Where possible, it should be attempted to implement the same solutions.

However, not all the materials that have been successfully applied in laser sintering will be similarly successful in the proposed process. Because the wavelengths at which the radiation is emitted are so vastly different, it is expected that the materials will show vastly differing absorptivity towards them. Another possible obstacle will be whether the radiative energy source and manner in which this energy is concentrated will meet the necessary criteria for spot size and power.

The energy provided by the sun should prove ample as, in South Africa, the average DNI is quite high. Provided a large enough lens of decent quality is used to concentrate the incoming radiation sintering rates should not be the limiting factor.

The way forward will be to, at first, validate the proposed thermal models. Once these have been validated possible material candidates can be chosen. Concurrently, the proposed lens should be tested to determine whether the criteria for power, necessary to ensure rapid sintering occurs, and spot size, necessary to ensure the products are created with a specified accuracy, are met. After this has been completed a prototype can be constructed and experimental tests can be performed. These should determine the effects of various process parameters, whether the physical model is indeed able to predict output properties and whether the overall process is possible.

3. Modelling

An attempt at sintering a powdered precursor material using solar energy has already been made by Rietma (2012). This was done by effectively replacing the dish of a parabolic dish collector with a Fresnel lens. The bed rotates underneath the lens to track the projection of the sun, while the lens attachment is constantly adjusted to face the sun. While such a system is capable of achieving high fluxes, due to only transmissive losses of the lens being present, the focal point is distorted from a circle to an ellipse at all times other than noon on specific days. This results in uneven heating as well as a lowered accuracy. The proposed set-up of the new 3D printer is almost identical to that of SLS except that, instead of a laser used as an energy source to sinter the powder, solar power is to be used. In general, however, this changes little. A radiative energy source is still used to systematically sinter specific regions of a powder bed, building up a component in layers. A highly simplified and idealised version of the setup of this process is shown in Figure 3.1.

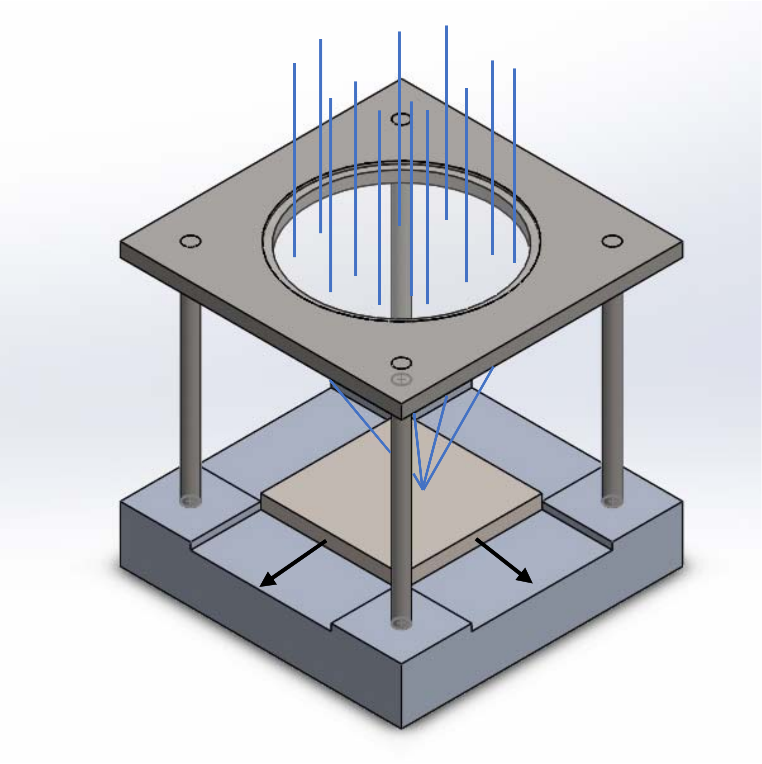

Figure 3.1: Simple Schematic of Proposed Printer

The lens should remain fixed as this is a bulky attachment while only the bed underneath should move. This can be controlled by stepper motors. Additionally, this arrangement eliminates the issue of an elliptical focal point.

The incoming radiation for this process is assumed to be already collimated. An arrangement of mirrors, controlled by a solar tracker, can be used to provide the maximal radiative flux throughout the day. A simplified schematic of what is required to achieve this is shown in Figure 3.2. The system requires at least two mirrors. The first receives light from the sun; this mirror must be adjustable in two directions in order to track the movements of the sun accurately. The light is reflected, parallel to the ground, onto a second, stationary mirror. This mirror reflects the light, perpendicular to the ground, onto the Fresnel lens. This removes the need to tilt the Fresnel lens in order to receive collimated light.

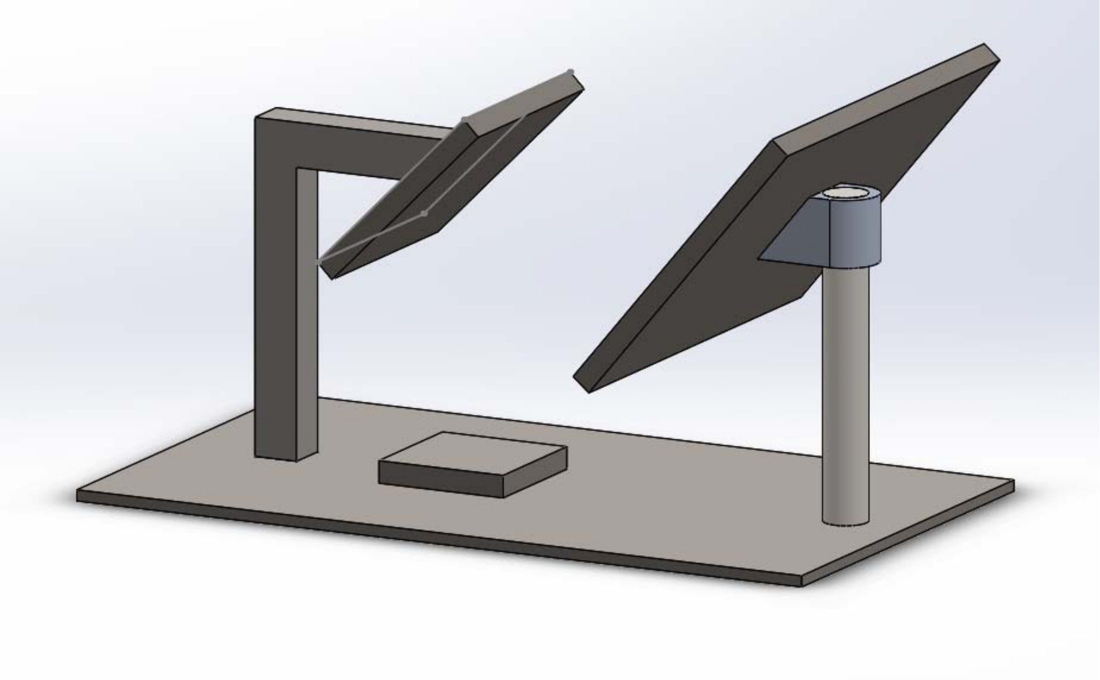

Figure 3.2: Simple Schematic of Proposed Concentrating Platform

The variables that affect this process can broadly be classified into three different categories: variables pertaining to the incoming radiation, variables pertaining to the printer and process and lastly variables pertaining to the material that is to be used for printing. The first category consists of variables such as: The incoming radiation flux and the spot-size of the lens. These are very difficult to control and will likely only be measured variables. The second category consists of variables such as the scanning velocity and the hatch spacing. These variables are inherently manipulatable and will be varied by adjusting settings on the printer. The third category consists of variables such as the heat capacity, bulk density and latent heat of fusion of the powder. While these properties are material characteristics, they can be manipulated by varying the composition of a material mixture. Because variables from different categories interact heavily in the printing process, being able to accurately model the values of these variables where they cannot be specified or measured is an integral component to being able to model the entire process successfully. Because of this, model equations need to be designed to predict both properties of the material as well as effective properties of the bed.

A Dimensional Analysis can aid in the understanding of the occurring phenomena during the printing process by determining how the variables of different categories interact. Here, instead of attempting to obtain a model function to link an output parameter of the process to input parameters, dimensionless parameters are generated. This reduces the number of variables required to completely describe the problem by the number of fundamental dimensions.

3.1. Dimensional Analysis

The Buckingham Pi theorem is the core theorem of dimensional analyses and a formalisation of Rayleigh's earlier work on dimensional analyses. The theorem is given by Brand (1957) as:

If an equation in n arguments is dimensionally homogeneous with respect to m fundamental units, it can be expressed as a relation between n – m independent dimensionless arguments.

This can also be summed up mathematically, where an output variable, y, is correlated to a number of input variables, x, through a function, f, as:

$$y = f(x_1, x_2, x_3, \dots, x_n) \tag{3.1}$$

The corresponding dimensionless variable π_y is then described by the equation:

$$\pi_y = F(\pi_1, \pi_2, \pi_3, \dots, \pi_{n-m}) \tag{3.2}$$

In doing so the complexity of the entire problem is potentially reduced. The individual dimensionless numbers can also help in the understanding of the system.

A large number of factors can influence the selective sintering process. According to Van Elsen, Al-Bender and Kruth (2008) more than 50 factors can easily be enumerated. However, a significantly simpler model can still yield valuable information on the process. The following dimensional analysis is conducted using the latent heat of fusion (λ), the spot size (d), the incident radiation power (P), the bulk density of the powder (ρ), the scanning velocity (v), the thermal diffusivity (α), the scan vector spacing (S_S), the layer thickness (L_t), the heat capacity (C_P) and the difference in temperature between ambient conditions and the melting point of the polymer (ΔT) as factors. Clearly the fundamental dimensions of the problem are: time, distance, mass and temperature. The velocity, the spot size, the incident radiation power and the temperature difference are chosen, arbitrarily, as repeating variables. The remaining variables are therefore core variables. Applying the Buckingham-Pi theorem to such a process can be cumbersome according to Osswald (2015:168). The Pawlowski matrix transformation method as used in Osswald (2015: 168) is therefore applied. As there are ten variables and four fundamental dimensions, six dimensionless groups are created in this manner. These six are:

$$\pi_1 = \frac{\lambda}{v^2} \tag{3.3}$$

$$\pi_2 = \frac{\rho\, v^3\, d^2}{P} \tag{3.4}$$

$$\pi_3 = \frac{L_t}{d} \tag{3.5}$$

$$\pi_4 = \frac{\alpha}{v\, d} \tag{3.6}$$

$$\pi_5 = \frac{S_S}{d} \tag{3.7}$$

$$\pi_6 = \frac{C_P\, \Delta T}{v^2} \tag{3.8}$$

Multiplying dimensionless numbers by one another results in new, valid dimensionless numbers (as a dimensionless model function). In this manner two new dimensionless groups can be created as:

$$\pi_7 = \frac{1}{\pi_1\, \pi_2 \pi_3} = \frac{P}{\rho\, d\, L_t\, v\, \lambda} \tag{3.9}$$

$$\pi_8 = \frac{1}{\pi_2\, \pi_3 \pi_6} = \frac{P}{\rho\, d\, L_t\, v\, C_P\, \Delta T} \tag{3.10}$$

These numbers are dimensionless forms of the energy equation, with Equation 3.9 describing the latent energy change of the process and Equation 3.10 describing the sensible energy change of the process. The reciprocal of Equation 3.9 has also been presented by Van Elsen et al. (2008) as the melting efficiency. Clearly, in this form, both equations are subject to a few assumptions:

1. Both Equation 3.9 and Equation 3.10 assume the material displays blackbody absorptivity.
2. Both Equation 3.9 and Equation 3.10 assume that no heat losses occur.
3. Equation 3.9 is approximately valid only if $\lambda \gg C_P \, \Delta T$.
4. Equation 3.10 is only valid if no part of the material undergoes a phase transition.

One would expect both dimensionless numbers to stay approximately constant, as an increase in incident radiation power or a decrease in scanning velocity would result in a thinner layer, compensating for the lower input power. Obviously to evaluate these dimensionless numbers, accurate knowledge of thermal properties, such as latent heat of fusion, heat capacity and melting temperature, as well as physical properties such as density, is a necessity. Being able to vary these properties continuously would be an additional benefit for the evaluation of these models. An important distinction must be made between the layer thickness of Equation 3.9 and that of Equation 3.10. The first accounts for the sintered depth; however, a greater depth will experience a sensible heat change.

3.2. Physical Model

The most common way of describing the heat transfer of the process is by reducing the energy balance to the Fourier heat conduction equation. This can be stated as:

$$\rho C_P \frac{\partial T}{\partial t} = \nabla(k\nabla T) + g(x,y,z,t) \tag{3.11}$$

This equation can be expanded to cartesian coordinates as follows:

$$\rho C_P \frac{\partial T}{\partial t} = \frac{\partial}{\partial x}\left(k\frac{\partial T}{\partial x}\right) + \frac{\partial}{\partial y}\left(k\frac{\partial T}{\partial y}\right) + \frac{\partial}{\partial z}\left(k\frac{\partial T}{\partial z}\right) + g(x,y,z,t) \qquad (3.12)$$

To solve the differential equation, initial and boundary conditions are necessary. These are stated as (Zeng et al., 2012):

Initial: $T(x,y,z,0) = T_0$

Surface: $-k\frac{\partial T}{\partial z}\bigg|_{z=surface} = \varepsilon\sigma\left(T^4 - T_{surr}{}^4\right) + h(T - T_\infty)$

Bottom: $-k\frac{\partial T}{\partial z}\bigg|_{z=0} = 0$

Clearly, it is assumed that the bottom of the bed is well insulated. The laser irradiation term, g— included here in Equation 3.11 and Equation 3.12— can either be added to the Fourier heat conduction equation or to the surface boundary condition. For the laser sintering of a titanium alloy this is illustrated by Figure 3.3.

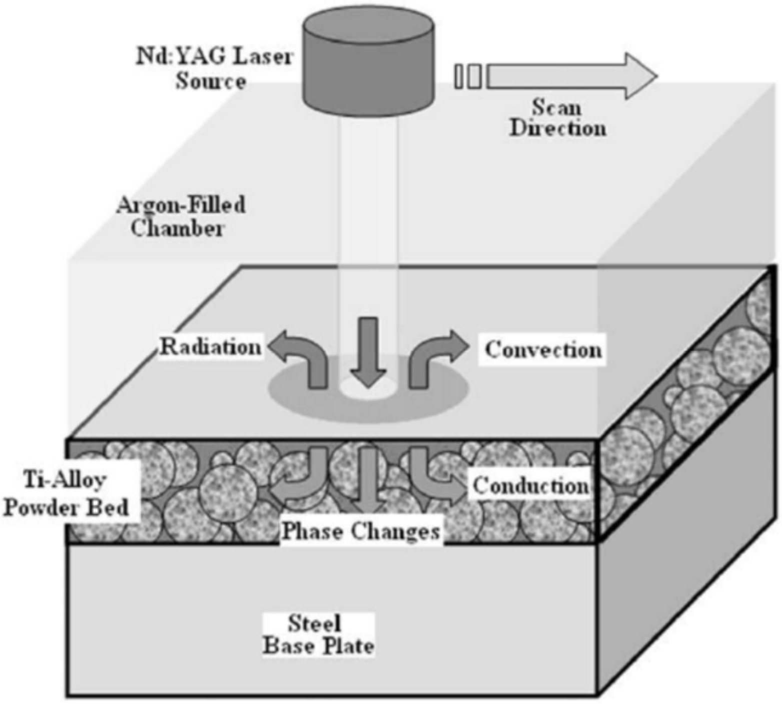

Figure 3.3: Schematic of Heat Transfer in the SLS Process (Zeng et al., 2012)

On the other hand, the total energy imparted into the sample can be expressed using integral relations. The integral form of the differential equation for energy transfer is given as (Welty, Rorrer, & Foster, 2014):

$$\frac{\delta Q}{dt} - \frac{\delta W_s}{dt} - \frac{\delta W_\mu}{dt} = \iint_{cs.} \left(e + \frac{P}{\rho}\right) \rho (v \cdot n) d + \frac{\partial}{\partial t} \iiint_{cv.} e\rho \, dV \qquad (3.13)$$

Where W_s refers to shaft work and W_μ refers to viscous work. At steady state Equation 3.13 can be simplified to read:

$$\dot{Q}_{radiation} = \dot{Q}_{sensible} + \dot{Q}_{latent} + \dot{Q}_{losses} \qquad (3.14)$$

where

$$\dot{Q}_{losses} = \dot{Q}_{reflective} + \dot{Q}_{conductive} + \dot{Q}_{convective} \qquad (3.15)$$

The energy density, considering both radiative power, spot size and velocity, can be expressed as (Simchi, 2006):

$$\mathrm{E} = \frac{\pi\eta P}{4dv} \tag{3.16}$$

However, because the scanning strategy is always set up in such a manner that the hatch spacing is smaller than the spot size, a certain degree of overlapping occurs. It is therefore necessary to differentiate between the energy density of a single track and the total delivered energy density. As the degree of overlapping is simply defined as the ratio of the spot size to the hatch spacing, the delivered energy density per unit area becomes:

$$\mathrm{E} = \frac{\pi\eta P}{4hv} \tag{3.17}$$

The assumption of this being a steady state problem is a reasonable one as all areas of the printed sample are treated equally and receive equal amounts of incoming radiation. Additionally, the process occurs so quickly that transient occurrences can be assumed negligible. By lumping reflective and conductive losses into a fraction of the incoming radiation, Equation 3.14 can be rewritten as:

$$aP = \rho(vdL_t)C_P(T_m - T_\infty) + \rho(vdL_t)\lambda + hd^2(T_m - T_\infty) \tag{3.18}$$

Here many parameters can either be specified— such as the velocity— or measured, such as the incident radiation, spot size and layer thickness. The heat transfer coefficient can be calculated from empirical relations; however, the heat capacity, latent heat of fusion and melting temperature must either be determined from literature or modelled. This equation still has two inherent assumptions. Firstly, that the material is initially at the temperature of the surroundings. This is a reasonable assumption to make as the material is stored along with the printer. The second assumption is that the heat losses occur at the melting temperature. Although this is strictly speaking not true as the heat losses will vary from none initially, up to the point where they are equal to the term in Equation 3.18. It is expected that this will not have a significant effect as the preheating step occurs rapidly. Equation 3.18 also contains a 'tuning parameter', a. This parameter is to account for losses that cannot be directly measured, such as the amount of radiation reflected by the material and the amount of incoming radiation refracted by the Fresnel lens. Provided the model has the correct shape, this parameter can be used to force the model to predict the correct outputs. This is useful for the design of a process control scheme.

Clearly Equation 3.18 is very similar to the summation of the two dimensionless numbers π_7 and π_8 obtained earlier. To verify this equation, it can be expressed to yield a value not specified by the operator - such as the printer scanning velocity - or fixed - such as the incoming radiation. A convenient choice would be the layer thickness, L_t. Rewriting Equation 3.18, one obtains:

$$L_t = \frac{aP - hd^2(T_m - T_\infty)}{\rho(vd)[C_P(T_m - T_\infty) + \lambda]} \tag{3.19}$$

Again, both Equation 3.19 and Equations 3.9 and 3.10 predict that $L_t \propto P \cdot v^{-1}$. This is to be expected: An increase in incident radiation will increase the total imparted energy (as per Equation 3.16 and Equation 3.17). In a similar manner an increase in scanning velocity will result in a decrease in the total imparted energy. A greater imparted energy will result in more material being sintered, increasing the layer thickness.

Assuming an effective thermal conductivity, the maximum temperature of the bed, found at the surface of the bed, can be expressed as (Zhang & Faghri, 1999):

$$T|_{z=surface}(t) = T_0 + \frac{q\sqrt{6\,\alpha_{effective}t}}{2\,k_{effective}} \tag{3.20}$$

The characteristic time it takes for the bed to reach its melting point is given by (Zhang & Faghri, 1999):

$$t_{mp} = \frac{2k_{effective}{}^2\left(T_{mp} - T_0\right)^2}{3\alpha_{effective}q^2} \tag{3.21}$$

The thermal layer thickness is given by Equation 3.22. It is proposed by Zhang and Faghri (1999) that the temperature distribution within the thermal layer has a quadratic dependence on the distance from the surface.

$$\delta_{mp} = \frac{2k_{effective}\left(T_{mp} - T_0\right)}{q} \tag{3.22}$$

Clearly, to evaluate these properties of the model, effective properties of the bed must be known. A variety of methods have been developed to calculate the thermal conductivity of a porous bed. Heat transfer is deemed to be due to conduction and radiation (Tolochko et al., 2003) . Convective heating is usually ignored as the pores are much too small to allow for significant fluid motion. However, conduction through the gas particles can still play a significant role. Tolochko *et al.* (2003) calculate the effective heat transfer coefficient as a sum of its conductive and radiative components:

$$k_{eff} = k_{radiation} + k_{conduction} \tag{3.23}$$

Where:
$$k_{radiation} = \frac{16}{3} L_P \sigma T^3 \tag{3.24}$$

L_P is usually in the order of the particle diameter (Tolochko et al., 2003). The conductive heat transfer coefficient is calculated by assuming that at small neck sizes— compared to the semi-infinite particle size—the contacts act independently. The flux through a particle is given by:

$$q = \frac{\Delta T}{s} \tag{3.25}$$

Where s denotes the thermal resistance. This quantity can be written as (A. V. Gusarov et al., 2003):

$$s = \frac{\Delta T}{k \int_0^b \left.\frac{\partial T}{\partial z}\right|_{z=s} 2\pi r\, dr} = \frac{1}{2kb} \tag{3.26}$$

The temperature difference can be rewritten as (Tolochko et al., 2003):

$$\Delta T = d|\nabla T| \tag{3.27}$$

The average area per particle contact is the side length of the lattice, a, squared, divided by the number of contacts:

$$A_{avg} = \frac{a^2}{N} \tag{3.28}$$

The average flux can now be rewritten by substitution of Equations 3.26 to 3.28 into Equation 3.25:

$$\frac{q}{A} = \frac{\Delta T}{sA} = \frac{2kbdN|\nabla T|}{a^2} \tag{3.29}$$

For most particle configurations the interlayer distance, number of contacts, as well as the lattice side lengths and ratios of tap density to actual density are known. Table 1 tabulates the results of the thermal conductivity in a vacuum for various packing configurations in terms of the density ratio of the bed and the neck size ratio.

Table 3.1: Dependence of Thermal Conductivity on Density and Contact Size Ratio (A. V. Gusarov et al., 2003)

	$\frac{\rho}{\rho_s}$	$\frac{k_c}{k_s \frac{b}{r}}$
FCC	0.74	$2\sqrt{2}$
BCC	0.6	$\sqrt{3}$
SC	0.524	1
Diamond	0.34	$\frac{\sqrt{3}}{4}$

As the bed is sintered the neck sizes grow. Tolochko *et al.* (2003) give a kinetic model describing the neck growth. It is shown in Equation 3.30:

$$\frac{d\left(\frac{b}{r}\right)}{dt} = \frac{1}{t_0}\left(\frac{b}{r}\right)^{-4} \tag{3.30}$$

With t_0 the characteristic time. It is possible to calculate this value; however, empirical tests must be conducted to calculate necessary constants. It should therefore be simpler to conduct tests on a sintering bed and fit a curve to the results.

A more empirical approach is taken by Bugeda, Cervera and Lombera (1999). Here, the combined effects of conduction in the gas and powder as well as radiation are expressed as using a model developed for the effective thermal conductivities in packed beds by Yagi and Kunii (1957) (as cited in Bugeda, Cervera and Lombera (1999)):

$$k_{eff} = \frac{\frac{\rho}{\rho_s} k_s}{1 + \varphi \frac{k_s}{k_g}} \tag{3.31}$$

with $$\varphi \approx 0.02 \cdot 10^{2\left(0.7 - \frac{\rho}{\rho_s}\right)} \tag{3.32}$$

A sharp transition takes place from the calculated effective thermal conductivity to the pure component thermal conductivity at the phase transition (A. V. Gusarov, Yadroitsev, Bertrand, & Smurov, 2007; Zhang & Faghri, 1999).

To calculate the effective thermal diffusivity of the unsintered bed, one simply divides the effective thermal conductivity by the volumetric heat capacity of the bed, considering the volumetric heat capacity of both the powder and the gas in the pores (Zhang & Faghri, 1999).

For the model to be accurate, convective heat losses from the top of the sintered part must be considered. As the process usually takes place in an enclosed area, natural convection is the dominant mode of heat transfer. The convective heat transfer coefficient for natural convection can be described using the Rayleigh number (Çengel and Ghajar, 2014: 539):

$$\mathrm{Ra} = \frac{g\beta(T_s - T_\infty){L_c}^3}{\nu\alpha} \tag{3.33}$$

This can be related to the Nusselt number for natural convection over a vertical plate, with the hot side facing up, as (Çengel and Ghajar, 2014: 540):

$$\mathrm{Nu} = 0.59Ra^{\frac{1}{4}} \tag{3.34}$$

For $10^4 < Ra < 10^7$. And (Çengel and Ghajar, 2014: 540):

$$\mathrm{Nu} = 0.1Ra^{\frac{1}{3}} \tag{3.35}$$

For $10^7 < Ra < 10^{11}$. The Nusselt number is defined as (Çengel and Ghajar, 2014: 540):

$$\mathrm{Nu} = \frac{\mathrm{h}\, L_c}{k} \tag{3.36}$$

The critical length, L_c, is calculated as (Çengel and Ghajar, 2014: 540):

$$\mathrm{L}_c = \frac{A_s}{p} \tag{3.37}$$

Where p denotes the perimeter.

3.3. Thermal Properties Model

It is well known for long that the melting point of a compound is strongly related to its latent heat of fusion. Work done in the late parts of the 19th century to early parts of the 20th century by Richards (1897) and Walden (1908), point to the two quantities being related by Equation 3.38 for a specific material group:

$$\frac{\Delta \mathrm{H}_{fus}}{T} = const \tag{3.38}$$

The constant value that relates the two properties is dependent on which material group is being described.

Having the ability to accurately predict the temperature at which a phase change occurs will therefore likely be a great advantage to predict the latent heat of fusion. To create an expression for the temperature at which fusion occurs an expression for phase equilibrium at specified conditions is usually used as a starting point. It may be stated that the fugacity of any component, i, must be equal in the liquid solution and in the solid solution (Smith, Van Ness and Abbott, 2005: 401; Walas, 2013: 160):

$$\hat{f}_i^{\,l} = \hat{f}_i^{\,s} \tag{3.39}$$

This expression can now be modified, using activity coefficients, to relate the fugacity of the pure components as:

$$x_i{}^l \gamma_i{}^l f_i{}^l = x_i{}^s \gamma_i{}^s f_i{}^s \tag{3.40}$$

By relating the fugacity to the Gibbs free energy and the Gibbs free energy to the enthalpy of fusion the following expression is generated (Smith, Van Ness and Abbott, 2005: 600):

$$\psi_i = \frac{f_i{}^l}{f_i{}^s} = e^{\frac{\Delta H_{fus,i}}{R\,T_{m,i}}\left(\frac{T - T_{m,i}}{T}\right)} \tag{3.41}$$

Equation 3.40 may now be substituted into Equation 3.41 and solved— either through knowledge of additional information or through simplifying assumptions— to obtain the temperature at which fusion occurs for a certain mixture of components. In the simplest case the assumption of ideal behaviour in the liquid phase and immiscibility in the solid phase ($\gamma_i{}^l$ = 1 and $x_i{}^s \gamma_i{}^s = 1$) result in the so-called Schröder (or Schröder-van Laar) equation (Walas, 2013: 408):

$$x_i = e^{\frac{\Delta H_{fus,i}}{R\,T_{m,i}}\left(\frac{T - T_{m,i}}{T}\right)} \tag{3.42}$$

In addition to ideal solution behaviour, this equation assumes that the heat capacities in the liquid phase and in the solid phase are equal. The Schröder equation creates a straight-line relationship for the equilibrium temperature between the liquid phase and the solid phase from the pure-component melting points to the eutectic temperature. The eutectic temperature itself can be calculated by noting that the component fractions in the liquid phase must sum to 1. Applying the Schröder equation results in a simple phase diagram as shown in Figure 3.4.

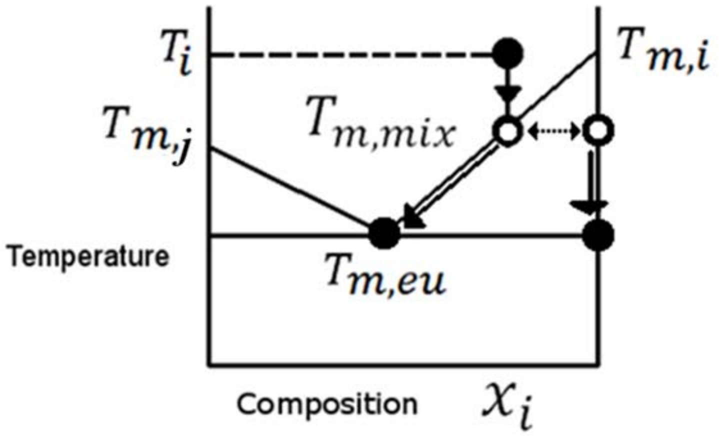

Figure 3.4: Simple Phase Diagram Displaying Eutectic Behaviour

Less ideal behaviour can be quantified in two increasingly complex ways. The accuracy can be improved by quantifying the non-ideal behaviour in the liquid phase whilst still assuming immiscibility in the solid phase. A further increase in accuracy should be noted if the assumption of immiscibility were replaced by a model describing the non-ideal behaviour of the solid phase. The activity coefficient can be calculated from (Smith, Van Ness and Abbott, 2005: 438):

$$\ln(\gamma_i) = \left.\frac{\partial n \frac{G^E}{RT}}{\partial n_i}\right|_{P,T,n_j} \tag{3.43}$$

This would require either a model for the Gibbs excess energy or an expression for the enthalpy of mixing. Both would require further information and limit the use of the resulting equation for performing quick predictions without the necessity for prior investigations. This expression can also not be applied if the assumption of an immiscible solid phase is not made, as its constraints are not met with.

Entropy is a state quantity and, as such, can be used to make closed cycle predictions. However, an even simpler method exists to make property predictions. The third law of thermodynamics states (Smith et al., 2005): *The absolute entropy is zero for all perfect crystalline substances at absolute zero temperature*. By having a known starting point for the entropy for all substances one can then calculate the entropy for two equivalent processes (Kosa, Proks, Strečko, Adamkovičová, & Nerád, 1993):

1. n component salts are heated from zero Kelvin to their individual melting points, where they undergo a phase transition. The salts are then cooled from their melting temperatures to the mixture melting temperature and mixed in the liquid phase.
2. A salt mixture comprising of n salts in the solid phase and at zero Kelvin is heated from zero Kelvin to the mixture melting temperature upon which it undergoes a phase transition.

These equivalent cases can be expressed mathematically as:

$$\sum_{i=1}^{n} x_i \left(\int_0^{T_{m,i}} \frac{Cp_{s,i}}{T} dT + \Delta S_{fus,i} + \int_{T_{m,i}}^{T_{m,mix}} \frac{Cp_{l,i}}{T} dT \right) + \Delta S_{mix} \tag{3.44}$$

$$\int_0^{T_{m,mix}} \frac{Cp_{s,m}}{T} dT + \Delta S_{fus,m} \tag{3.45}$$

The Neumann-Kopp law is now utilised to relate the mixture heat capacity to the individual heat capacities. Equating Equations 3.44 and 3.45 and employing this law, the expression, as found in Kosa *et al.* (1993), is generated:

$$\mathit{\Delta} S_{fus,m} = \sum_{i=1}^{n} x_i \left(\int_{T_{m,mix}}^{T_{m,i}} \frac{Cp_{s,i} - Cp_{l,i}}{T} dT + \mathit{\Delta} S_{fus,i} \right) + \mathit{\Delta} S_{mix} \tag{3.46}$$

The Gibbs free energy is defined as:

$$G \equiv H - TS \tag{3.47}$$

The Gibbs free energy is defined to be equal to zero for an equilibrium process, such as a phase transition. One may therefore write:

$$\Delta S_{fus} = \frac{\Delta H_{fus}}{T} \tag{3.48}$$

For a constant temperature process—such as mixing— the associated change in entropy is given by

$$\Delta S_{mix} = \frac{\Delta H_{mix} - \Delta G_{mix}}{T} \tag{3.49}$$

Two applicable equations relating the Gibbs excess energy and Gibbs free energy of mixing are (Smith, Van Ness and Abbott, 2005: 418, 450):

$$\frac{G^E}{RT} = \sum_i x_i \ln \gamma_i \tag{3.50}$$

$$G^E = \Delta G_{mix} - RT \sum_i x_i \ln x_i \qquad (3.51)$$

Equations 3.50 and 3.51 can now be substituted into Equation 3.49 and the resulting expression and Equation 3.48 substituted into Equation 3.46 to yield:

$$\Delta H_{fus,m} = T_{m,mix} \sum_{i=1}^{n} x_i \left[\frac{\Delta H_{fus,i}}{T_{m,i}} - R \ln(\gamma_i x_i) \right] + \Delta H_{mix} \qquad (3.52)$$

Equation 3.52 is based on the assumption that melting occurs at a single temperature. However, for any mixture that is not at eutectic conditions this is not the case. As the mixture melts the melting temperature will vary from an initial point above the eutectic temperature until it reaches the eutectic temperature. In most cases however, the variance between component melting temperatures and the eutectic temperature is small and this effect can be safely ignored.

The ideal solution theory assumes that the heat of mixing is negligible and that behaviour in the liquid phase is ideal. With these assumptions the entropy of mixing becomes:

$$\Delta S_{mix} = -R \sum_i x_i \ln x_i \qquad (3.53)$$

Therefore, for the ideal case, Equation 3.52 can be rewritten as:

$$\Delta H_{fus,m} = T_{m,mix} \sum_{i=1}^{n} x_i \left[\frac{\Delta H_{fus,i}}{T_{m,i}} - R \ln(x_i) \right] \tag{3.54}$$

This equation, coupled with the Schröder-van Laar equation to relate the melting temperature to the composition under consideration, can be used to make predictions of the latent heat of fusion and the temperature at which fusion occurs based only on pure component properties that are easy to measure, i.e. the melting temperature and the latent heat of fusion of the pure components.

4. Experimental Design

4.1. Printer Design

To conduct experiments, it was first necessary to have a working prototype printer. Initially it was thought that, by modifying an off-the-shelf FDM printer, a suitable prototype could be created. This would be done by mounting a lens attachment to the hot end or extruder head of the printer. However, the bulkiness of the lens attachment meant that the printer became imbalanced leading to a decrease in print quality. Additionally, because of the shift in focal point from the original print location, the bed size would have been so severely decreased that creating samples of a suitable size would be practically impossible.

Building a simple printer by hand resulted in inaccuracies that rendered the stepper motors underpowered and caused vibrations that decreased the quality of the print and proved disastrous for the mechanical integrity of the printer over time. It was therefore decided to machine a printer based on a CAD design. The material of construction was initially chosen to be thick wood. The thickness was chosen so as to limit the effect of warping due to the large variances in temperature incurred during testing, whilst keeping the printer both cheap and lightweight.

Because of the bulkiness of the lens and its mount, it was decided to keep these fixed while only controlling the movements of the bed below. The bed was decided to be 320 mm by 245 mm in size. This would be large enough to conduct tests and is comparable to small 3D printers intended for home use. Chromed steel fittings were specified in order to reduce friction, thereby increasing the lifespan of the printer and the quality of produced prints.

An Isometric CAD drawing of the designed prototype printer can be seen in Figure 4.1.

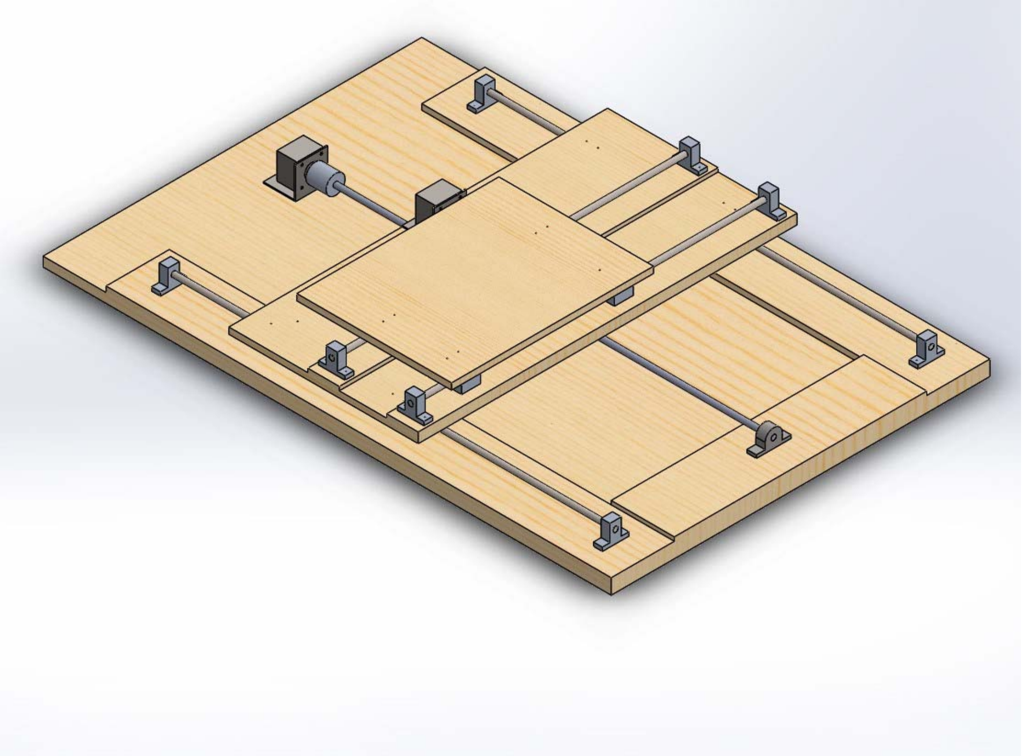

Figure 4.1: Isometric CAD drawing of 3D Printer

Control of the x-direction was decided to be actuated via a rail while control of the y-direction was to be actuated via a threaded rod. In doing so, the stepper motors could be aligned, allowing for easier wiring to the controller. The control of the different axes is visible from the orthographic drawing, shown in Figure 4.2.

The rail causes a movement of 40 mm per revolution of the motor, while the rod causes a movement of 8 mm per revolution. These parameters are necessary in order to calibrate the control system. While the rod allows for much more precise control over the printer movements, it is expected that the rail is more than sufficiently accurate.

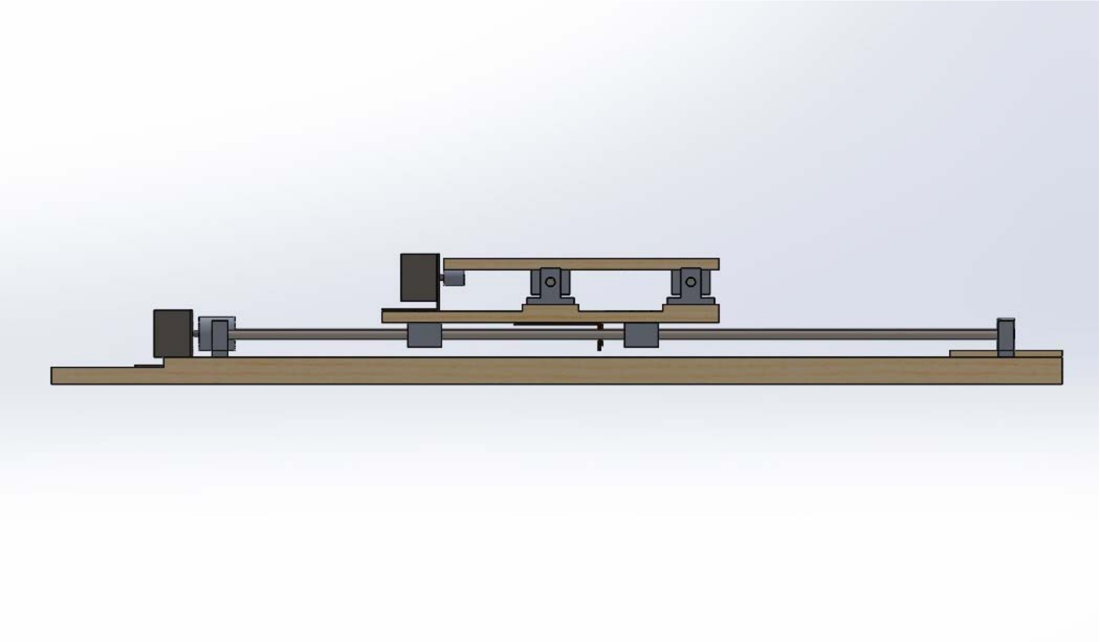

Figure 4.2: Orthographic CAD drawing of 3D Printer

4.2. Control System

To control the printing process an Arduino Mega R3 microcontroller was used in conjunction with two TB6600 stepper motor drivers. These drivers can deliver up to 4 A each. Additionally, they are equipped with large heat sinks, necessary to prevent overheating during operation. Wantai NEMA 17 stepper motors with a holding torque of 4000 g·cm were chosen as they were deemed able to accelerate the printing bed sufficiently. Because stepper motors have no intrinsic way of determining their own position homing switches were used to home the printer upon start-up and then move to a designated position close to the centre of the printing bed to await the printing procedure. Should the stepper motors skip steps due to an issue such as an obstacle or an error in the code execution, the motors would have to be re-homed.

A small 16 by 2 character screen was used to interface with the motors. This allowed for quick modifications to: the printed sample size, the scanning velocity and the acceleration. A setting to move the printer to its original location, or home it if necessary, was also included.

The assembled printer— with fittings, microcontroller, motor drivers and motors— and suspended within the rig, is shown in Figure 4.3. The total cost for this system amounted to about US$ 1000.

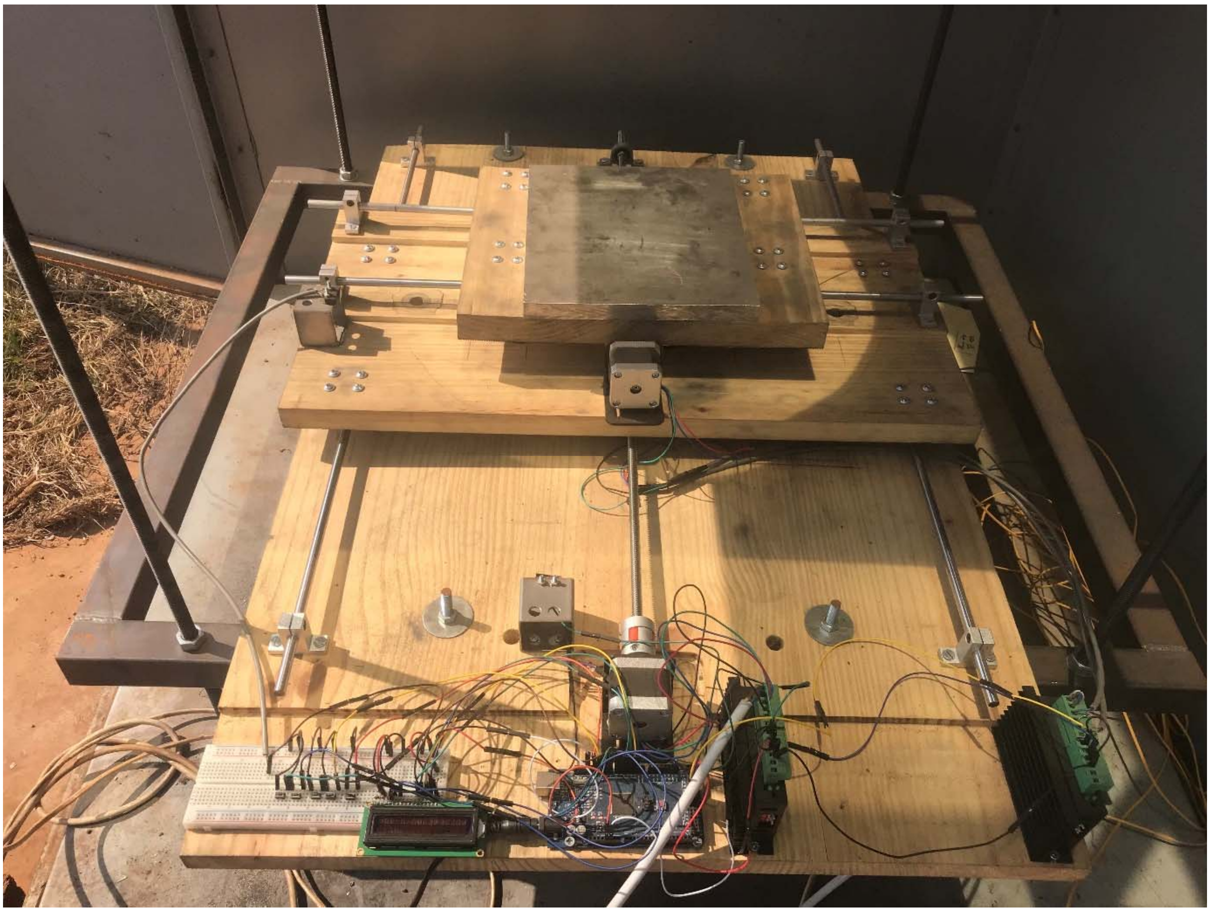

Figure 4.3: Photo of Constructed 3D Printer

4.3. Concentrating Platform

The power for the printer is derived from solar radiation and needs to be delivered to the printer in the form of collimated light. A rig on the experimental farm of the University of Pretoria had the necessary equipment for this task.

The rig uses two mirrors to collimate sun light: a primary, collecting mirror and a secondary, collimating mirror. The primary mirror has a two-axis control system linked to four photodiodes— one for every direction— which provide measurements for feedback control. The system can either be set to automatically track the sun or be manually adjusted by the operator. Light is reflected from the primary mirror, parallel to the ground, onto the secondary mirror which collimates it and reflects it onto the Fresnel lens of the printer below. The rig is therefore similar to a "power tower" operating on a single heliostat. The concentrating platform on the experimental farm is shown in Figure 4.4.

Figure 4.4: Constructed 3D Printer Mounted in Concentrating Platform

The Fresnel lens has an aperture diameter of 470 mm, a focal length of 460 mm and concentrates the solar energy onto a focal spot of roughly 3 mm. This gives the lens a concentration ratio of roughly 24 500. The Fresnel lens was supplied by Edmund optics (Stock #46-392, Edmund Optics, UK).

Because of possible misalignments of the collimating mirror it was decided to suspend the printer from four threaded rods inside the tower as opposed to merely placing it on the floor. This allowed the printer to be adjusted in all directions in order to optimise the size of the focal point. While the x- and y-axes are automatically controlled by the micro-controller, to control the printer in the z direction the threaded rods have to be adjusted manually. This is necessary due to the incoming radiation having a 'conical' profile. Unlike a conventional SLS printer, by adding layers without adjusting the height between the bed and the lens, the incoming energy density would be reduced. A ray-tracing schematic, showing the path of the light, is shown in Figure 4.5.

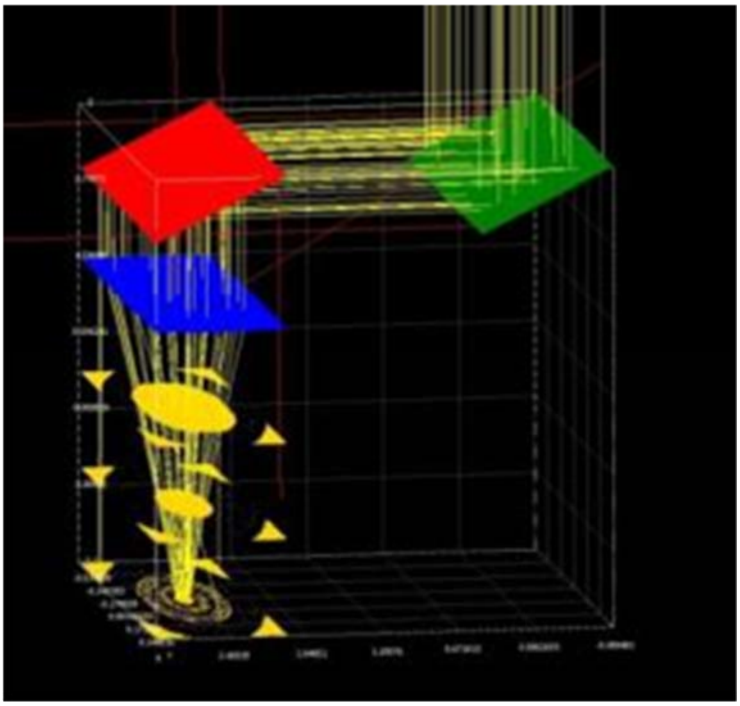

Figure 4.5: Ray Tracing Schematic of Solar Collector

4.4. Characterisation

The incoming radiation was quantified using an Apogee MP-200 hand-held pyranometer and three Apogee SP-215 pyranometers. The latter produce a 0 V to 5 V signal which can be directly interfaced with an Arduino after calibration with the hand-held pyranometer. The SP-215 pyranometers were laid out in 120˚ intervals around the Fresnel lens, starting from the northern most point of the lens, in order to get accurate measurements of the incoming solar radiation. Both types of pyranometers use a calibrated silicon-cell photodiode with a specified accuracy of 95 %. They are capable of quantifying radiation from 0 W·m^{-2} to 1250 W·m^{-2} within the spectral range of 360 nm to 1120 nm.

To measure the thickness of the prepared samples a sheet-metal micrometer was used. This has a manufacturer specified accuracy of 0.01 mm.

A Carl Zeiss optical microscope was used to inspect the printed samples in order to evaluate what type of sintering had taken place, through the created microstructure. Microscope images were taken at 5, 10- and 20-times magnification.

4.5. Process Control

The standard block diagram for feedforward-feedback control according to (Seborg, Mellichamp, Edgar, Doyle, & Iii, 2004) can be seen in Figure 4.6 below.

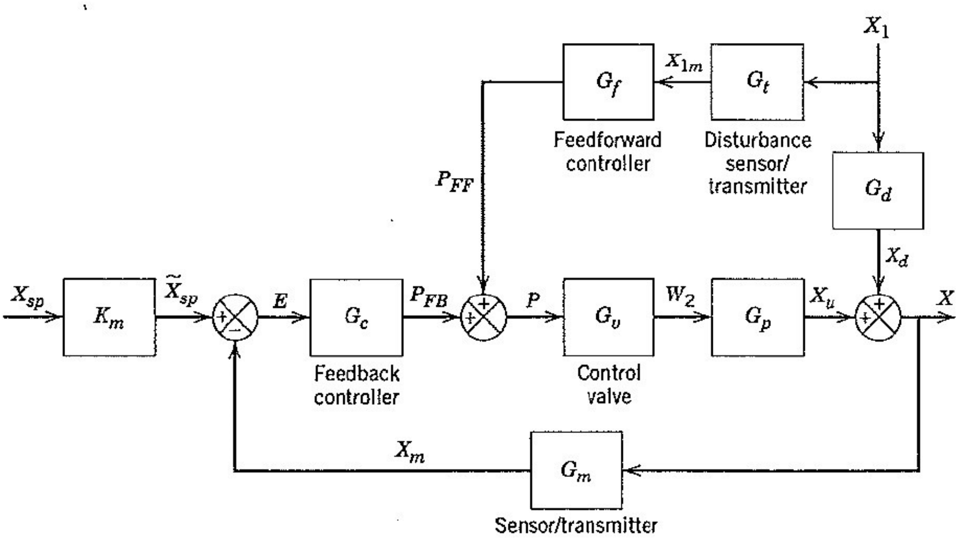

Figure 4.6: Block-flow Diagram for Feedforward-feedback Control (Seborg et al., 2004)

While this figure is technically meant to describe a chemical process controlled through the actuation of a control valve, through similarities it is applicable to the current process. The layer thickness, $L_{t,}$ was chosen as the controlled variable, as Equation 3.19 can be used as a model equation to control the process. Although the solar irradiation is the variable most essential to the operation of the printer, in this case it was labelled as a disturbance variable due to its uncontrollable nature and impact on the process. Measuring the layer thickness of a particular printed track during a printing run is essentially impossible to do accurately, reliably or quickly enough to be useful. This makes feedback control an unrealistic option. Therefore, feedforward control was used by measuring the incident radiation and calculating the required scanning velocity to obtain the desired layer thickness. Should the model be accurate, this will provide satisfactory results. However, if factors unaccounted for by the model play a significant role, the control system will fail due to the inability to measure the controlled variable. The model accuracy was evaluated prior to its implementation as a control system. The same Arduino Mega used previously to test the system was recoded as the feedforward controller.

4.6. Testing Procedure

The first step was to characterise the concentrating platform in terms of the amount of radiation it received and how efficiently it is able to concentrate this radiation. This was done on cloudless days as the printer can only be operated at reasonably high DNI.

To allow the testing of various factors on the process the predictive salt model was employed in order to generate salt mixtures that mimicked the properties of materials commonly employed in the SLS process. The model was first verified against data from literature in order to ascertain its applicability.

Only 2D tests were conducted. This was to determine the validity of the developed models. The tests were conducted by depositing a powdered material with a known mean particle size onto the movable bed and scanning over the powder at a predetermined velocity. Once this had been done the samples were cooled to ambient conditions and then analysed. The results were then used to evaluate the model and determine a suitable tuning parameter. This was then used to develop the process control scheme.

5. Results and Discussion

5.1. Thermal Properties Model

As the solution of the enthalpy of fusion model is predicated upon an accurate model for the temperature at which fusion occurs, this was considered first. To evaluate whether the model is accurate the model results were compared to the properties of 21 binary salt eutectics, documented by Kenisarin (2010). This was deemed sufficient to comment on the accuracy of the model.

The results of the eutectic temperature prediction for the Schröder-van Laar equation can be seen in Figure 5.1 below. Temperatures reported here are normalised to the maximum temperature.

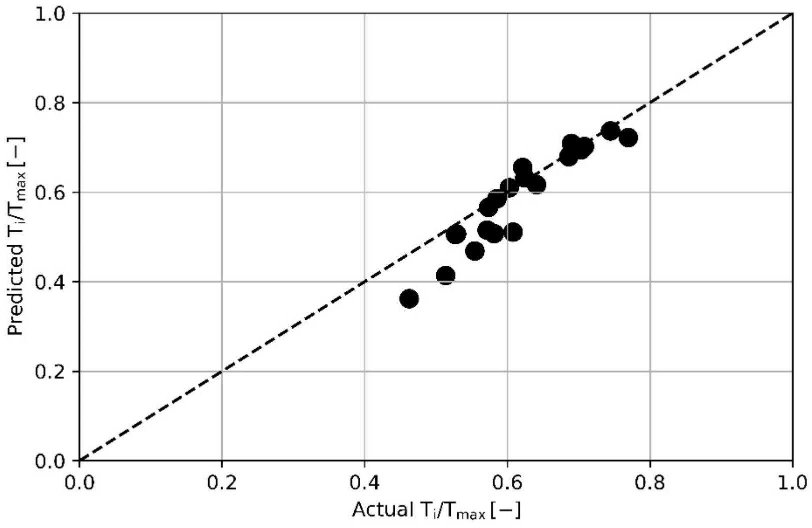

Figure 5.1: Predicted vs Actual Relative Eutectic Temperatures

An RMS error of 12 % indicates that the calculated values agree very well with measurements and therefore this is a very good first guess for the eutectic temperature, relying only on the melting temperatures and latent heats of pure components to make the estimation. The eutectic fractions, implicitly calculated through the eutectic temperature, for the same group of salts, are shown in Figure 5.2.

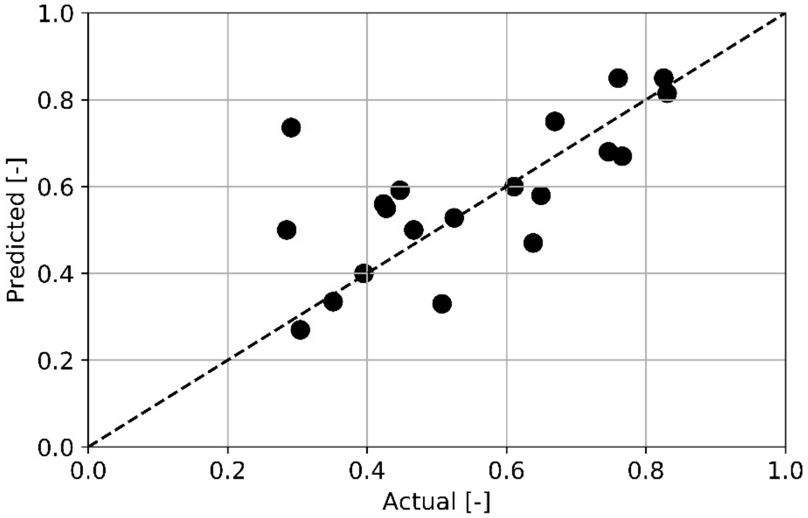

Figure 5.2: Predicted vs Actual Eutectic Fractions

The RMS error for this property estimation is slightly worse, at 25.5 %. The comparatively larger error is likely due to the curvature of the typical real phase diagram, where liquidus temperatures close to the eutectic temperature can be found over a broad range of compositions. The eutectic temperature therefore has a much higher chance of being predicted correctly than the eutectic fraction.

In order to improve the accuracy of predictions it is possible to utilise an expression for the excess energy to calculate an activity coefficient, describing non-ideal behaviour in the liquid phase, as per Equation 3.41. An expression for the excess energy, such as the Wilson equation, can now be fitted to the data in order to precisely predict eutectic conditions by calculating the Wilson parameters at the eutectic point. Not only does this force the eutectic temperature to be predicted with no error, but the accuracy for all compositions is improved by adding curvature to the straight lines predicted by the Schröder equation. However, if one now plots the excess energy for the entire composition, as is done in Figure 5.3 for the $NaNO_3$-KNO_3 system, inconsistencies become apparent. Here, the excess energy is plotted against composition for the fitted result and a curve resulting from experimental values determined by Kleppa (1960).

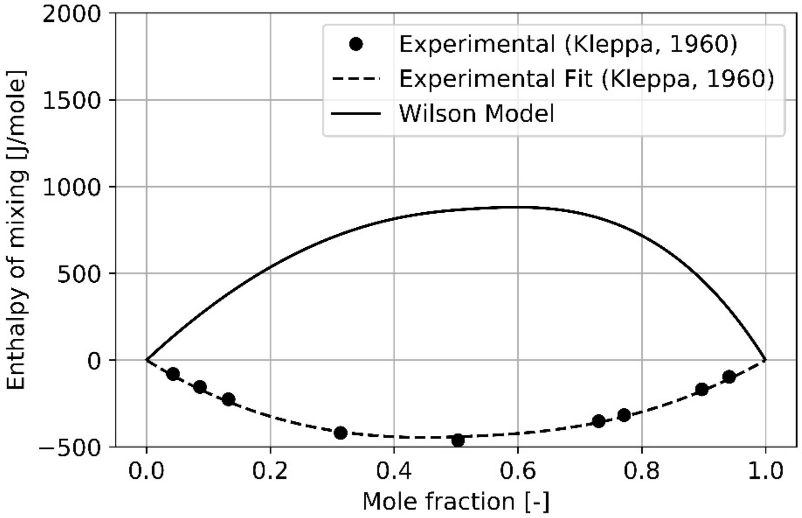

Figure 5.3: Calculated and Experimentally Determined Enthalpies of Mixing

Clearly a completely incorrect result is obtained, showcasing the potentially disastrous result when fitting a model to data that the model doesn’t explicitly predict. On this basis it was decided to neglect excess Gibbs energy equations that provide an activity coefficient to model the liquidus temperature. Figure 5.4 shows the comparison between the entropic enthalpy of fusion estimating approach and data obtained from literature for the case of the $NaNO_3$-KNO_3 system.

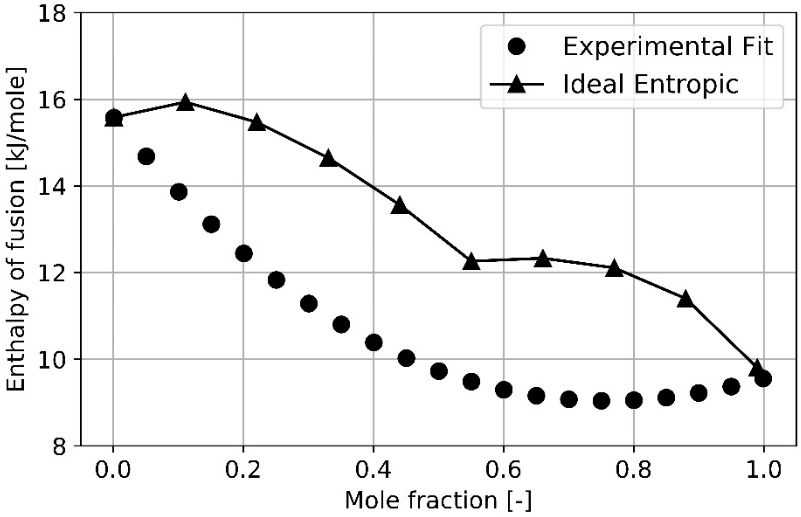

Figure 5.4: Enthalpy of Fusion, Prediction vs Actual

Because data from literature varies considerably— up to 20 %— a curve that minimises the error was fit to both data obtained from literature and DSC tests performed for the current study. A poor prediction is observed, with the inflection of the curve tending in the opposite direction to what is expected. It was found that the contribution of the entropy of mixing term of Equation 3.54 has a significantly greater effect than it should, probably due to it being multiplied by the melting temperature of the salt mixture. By simply omitting this term a modified entropic approach, illustrated by Equation 5.1, is created (Badenhorst & Böhmer, 2018):

$$\Delta H_{fus,m} = T_{m,mix} \sum_{i=1}^{n} x_i \left(\frac{\Delta H_{fus,i}}{T_{m,i}} \right) \tag{5.1}$$

The effects of this approach, in conjunction with the Schröder van-Laar equation to relate melting temperature of the mixture to the composition can be seen in Figure 5.5.

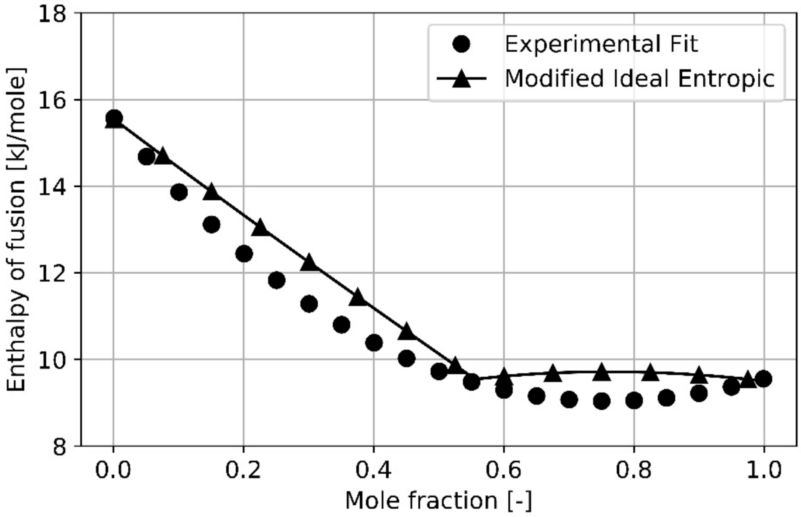

Figure 5.5: Enthalpy of Fusion; Predicted vs Actual for Modified Entropic Approach

Clearly, a significant improvement can be seen when comparing Figure 5.5 to Figure 5.4. This should provide the ability to make reasonable first estimates based only on pure component property information to effectively ‘screen’ wide ranges of compounds for suitable candidate compounds. However, to test the applicability of this approach its accuracy was tested against the same salt combinations used earlier. The results of the latent heat of fusion prediction using this modified entropic approach are shown in Figure 5.6.

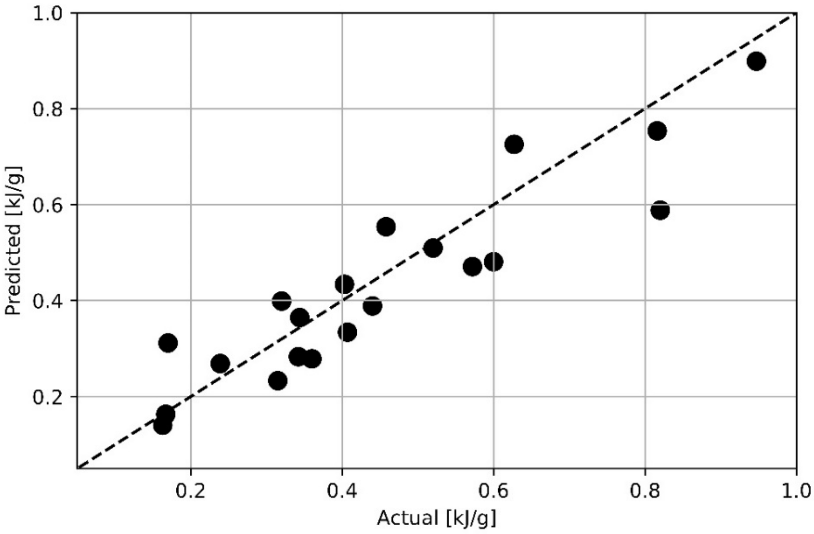

Figure 5.6: Predicted vs Actual Latent Heat of Fusion

A reasonably good fit is observed with an RMS error of 24.7 %. The most important thermal properties of a salt mixture can therefore be predicted in this manner, using only pure component properties.

The latent heat is not as widely documented as melting temperatures. The model's reliance on this parameter can be negated by employing the work done by Richards (1897) and Walden (1908). Plotting the latent heat of fusion against the melting point for various ionic compounds one obtains Figure 5.7.

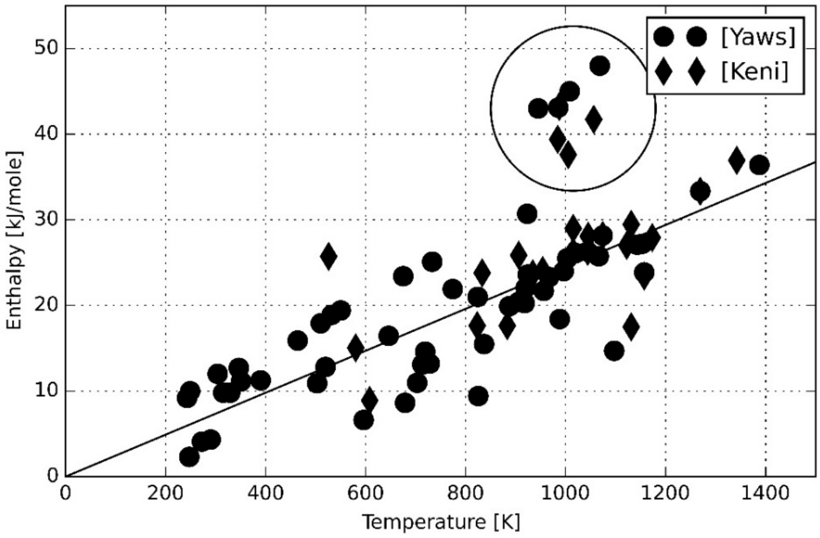

Figure 5.7: Latent Heat of Fusion vs Melting Point for Ionic Compounds

Most compounds follow the trend, known as “Richards’ Rule”, well, with a slope of approximately 24.5 J·mol^{-1}·K^{-1}. A clear group of outliers— encircled in Figure 5.7— is identifiable. This group consists of divalent metal halide salts. These clearly have a significantly higher molar enthalpy of fusion than the rest, illustrating how care should be taken with this approach as it is not necessarily always applicable. However, the trend of the above relation is very clear. This allows for it to be used in conjunction with the Schröder- van Laar equation and modified entropic approach to make predictions of the eutectic and liquidus temperatures, the eutectic composition and the latent heat of fusion using only melting temperatures of the pure components. Figure 5.8 shows the comparison between the predicted and measured latent heat of fusion at the eutectic point using this approach.

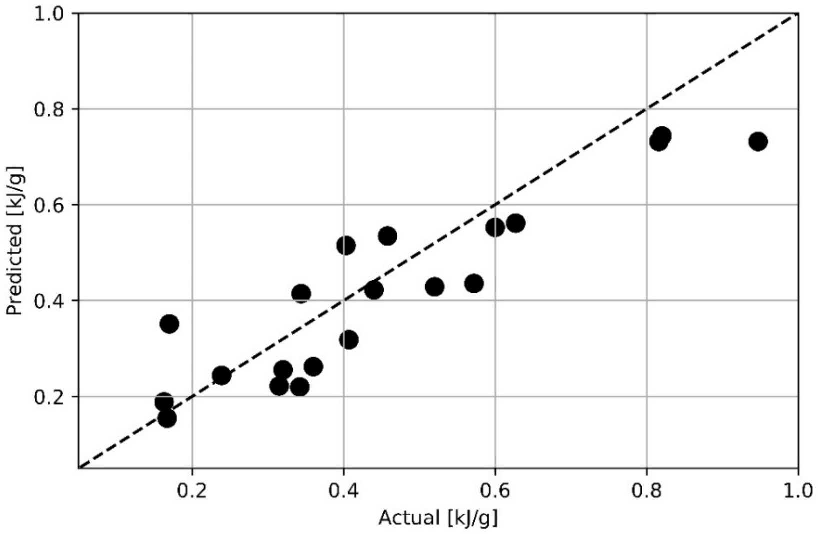

Figure 5.8: Predicted vs Measured Latent Heat of Fusion Using Richards' Rule

The RMS error for this approach is increased slightly to 30.6 %. However, these predictions now rely solely on the melting points of the individual compounds, making for a reasonable first guess when extensive material properties are not readily available.

5.2. Concentrating Platform Characterisation

The radiative energy losses of the concentrating system are shown in Table 5.1. The measurements of this table were taken immediately after the mirrors were cleaned. It must be noted that the mirrors became dusty quickly— partially due to nearby construction— and long-term usage without cleaning the mirrors was not a possibility.

Table 5.1: Radiative Energy Losses of Concentrating Platform

Concentrator	Losses
Collecting (Mirror 1)	34 %
Collimating (Mirror 2)	30 %

The values of the losses, measured around noon over multiple days, varied by approximately as much as the measuring inaccuracy of the handheld pyranometer. Clearly, the total losses, merely over the mirror, amount to approximately 54 %. The Fresnel lens has a manufacturer specified transmission of 92 %. This, however, will be compensated for in the heat transfer model. Nevertheless, a sizable fraction of the incoming radiation is lost, lowering the efficiency of the process and limiting the speed at which printing can be done.

The feedback control system of the mirrors uses four photodiodes, coupled with an optimisation scheme to position the collecting mirror. This optimisation scheme moves the collecting mirror in steps after a large enough change in radiation has been measured by one of the photodiodes. These sudden step changes, as opposed to continuous tracking, proved disastrous for the printing procedure. A small adjustment by the collecting mirror created a large change in the position of the focal point of the Fresnel lens. This has the potential to ruin a print. For the current tests it was therefore decided to manually control the collecting mirror, position it centrally and allow it to drift during printing tests. The mirror was then repositioned in between tests. This produces a gradually increasing error that can be ignored more safely than the large error caused suddenly through action of the control system.

5.3. Two-Dimensional Tests

Using the salt property model described earlier, it was determined that a eutectic mixture of $NaNO_3$ and KNO_3 would have roughly similar properties to the Nylon 12 used in SLS. One difference between the two, however, is their absorptivity to broadband radiation. Nylon SLS can be manufactured in any colour and tailored to absorb the incoming radiation. The salt combination, naturally colourless, was modified to increase its absorptivity to solar radiation. To do so, 2 % by mass carbon black was added to the salt mixture. This created a grey mixture with seemingly similar optical characteristics to commercial SLS polymer powder.

The predicted and actual properties and those of Nylon 12 are shown in Table 5.2. The heat capacity of the salt mixture was calculated using the Neumann-Kopp relation.

Table 5.2: Summary of Relevant Material Properties (Kenisarin, 2010; Vasquez, Haworth, & Hopkinson, 2011):

	$NaNO_3$ - KNO_3 Predicted	$NaNO_3$ - KNO_3 Literature	Nylon 12
Latent Heat of Fusion	114.7 $J·g^{-1}$	117 $J·g^{-1}$	96.7 $J·g^{-1}$
Melting Point	185.3 ˚C	222 ˚C	180 ˚C
Heat Capacity	1.4 $J·g^{-1}·K^{-1}$	-	1.7 $J·g^{-1}·K^{-1}$

The latent heat of fusion of the salt is very similar to that of the Nylon, differing by approximately 17 %. While the heat capacity and melting point differ, they differ in a manner such that the total sensible energy change, incurred during the preheating phase, varies only by about 3 %. This should have the effect that approximately equal time is spent in the first phase of the sintering process for the two different materials.

5.3.1. Salt Tests

In order to recreate realistic conditions, a eutectic composition of sodium- and potassium nitrate were milled down in order to obtain a mean particle size close to that of commercial SLS. This is usually approximately 40 μm. The achieved particle size distribution is given in Table 5.3 below.

Table 5.3: Salt Particle Size Distribution

Upper Size (μm)	Lower Size (μm)	Mean Size (μm)	Mass Salt (g)
212	125	168	17.12
125	75	100	67.65
75	45	60	142.3
45	32	38	149.9
32	25	28	3.58

The mean particle size was found to be 63 µm. Although this is slightly larger than commercial SLS powder, the difference is expected to be minimal. Care was taken in order to ensure that the layer thickness did not become too small, thus adhering to the rule proposed by Bertrand *et al.* (2007).

The mean of the dimensionless number, π_7, for these tests was 7.06 with a variance of 0.03. However, these statistics do not completely describe the process. The thickness used in the calculation of the dimensionless number is an average thickness of the sintered part. The individual thickness measurements for a single sintered part varied by up to 20 %. This is due to the rigidity of the salt, solidifying with defects on the surface, which skew the measuring process. However, because the average does give a representation of the amount of material sintered the statistics still show a good fit and that the model accurately describes the process. The dimensionless number is only a function of the absorptivity of the powdered material and similar results should therefore be expected for tests with an absorptive SLS polymer. The high value of the number indicates a low melting efficiency, probably due to not all the radiation being absorbed as heat and no attempt being made to limit convective and conductive losses.

Problems with effects akin to those produced by the balling effect were noted in tests where the salt was not milled down sufficiently. The increase in distance between adjacent particles of a higher mean particle size resulted in the complete melting of individual particles which would subsequently coalesce and form molten droplets. While this issue is severe and leads to a substantial decrease in print quality due to the incorrect sintering of a given layer and the inability of any succeeding layers to sinter correctly with that layer, it is easily avoidable if a powder consisting of correctly sized particles is used.

An additional problem was an extremely brittle final part. This is characteristic for crystalline, ionic substances. Extreme care had to be taken not to break the final sintered part during its analysis.

5.3.2. Polymer Tests

Polymer tests were now conducted in a similar manner, producing 10 cm x 10 cm sheets of varying thicknesses. The thickness of the sheets varied from approximately 200 µm to approximately 1500 µm. An example of the sheets can be seen in Figure 5.9 below.

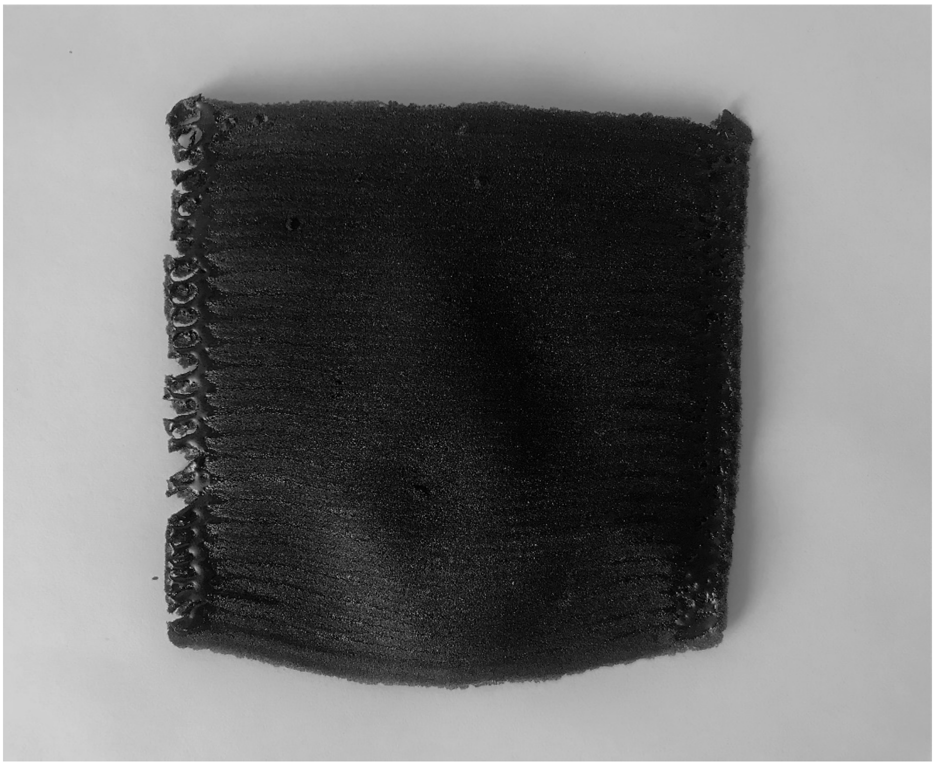

Figure 5.9: Sintered Polymer Sample

Noticeable in the sample is the sintered centre but molten and even thermally degraded edges. This is due to the scanning strategy of the printer: from an initial standstill its velocity increases to a maximum. This velocity is then maintained over a large portion of the scan vector length. The bed is then slowed down again to come to a standstill at the end of the specified distance. After which the bed is moved in the perpendicular direction by the hatchspacing. During this deceleration and readjustment period the scanning velocity was relatively low, increasing the imparted energy and causing the polymer to melt. In most cases the maximum velocity was maintained over ~ 95 % of the track distance, allowing for accurate measurements near the centre of the sample.

Microscope tests were performed on the samples at 5-, 10- and 20-times magnification. Based on the results of these tests the samples could be divided into two groups: samples in which only sintering occurred and samples in which both sintering and melting occurred. An example of the three microscope images for a sample in which only sintering occurred can be seen, in grayscale, in Figure 5.10.

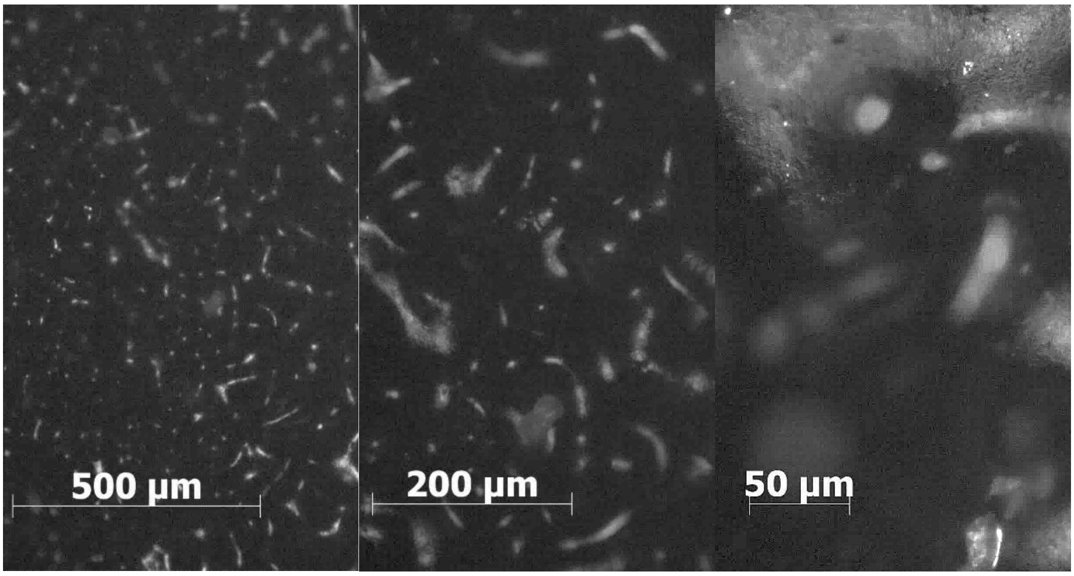

Figure 5.10: (From Left to Right) Sintered Sample at 5-, 10- and 20- Times Magnification

At 5 times magnification it was easiest to determine to what degree the sample had melted. At 20 times magnification individual, unsintered particles were clearly be seen. These were roughly spherical and 40 µm in size. A sample which had undergone both sintering and melting can be seen in Figure 5.11 at 5- and 10- times magnification.

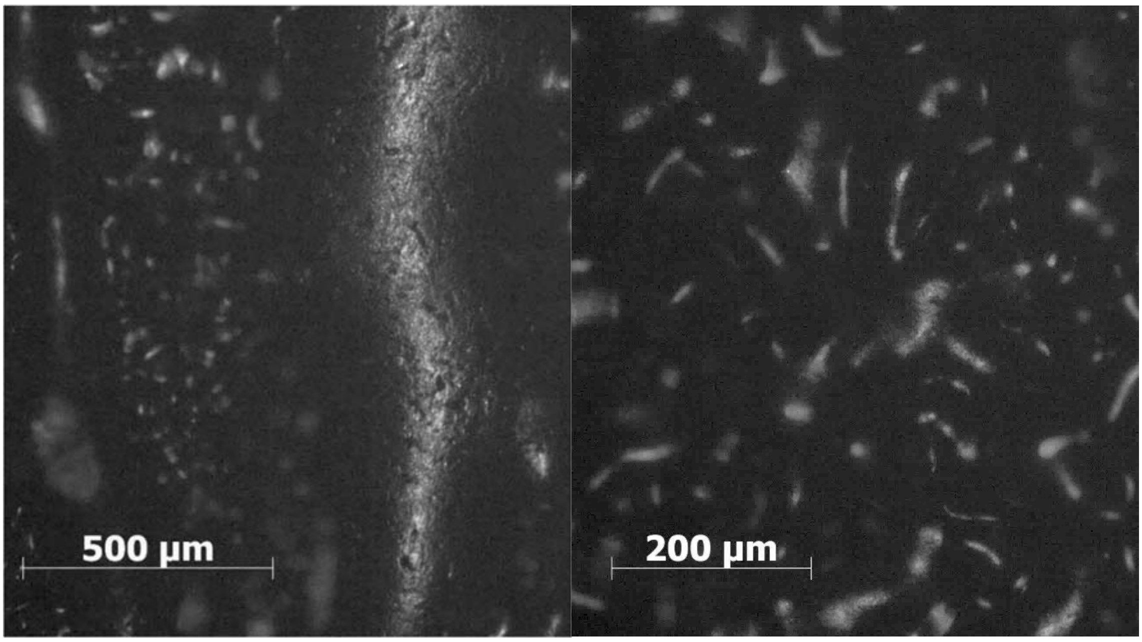

Figure 5.11: Sample which has Undergone both Sintering and Melting (Left: 5x, Right: 10x)

The melt track is clearly visible in the figure magnified to 5 times its ordinary size, indicating liquid state sintering, as opposed to the solid state sintering in Figure 5.10.

5.3.3. Dimensional Analysis

Plotting the variables of the dimensionless number, π_7, against the scan speed the following Figure, 5.12, is generated.

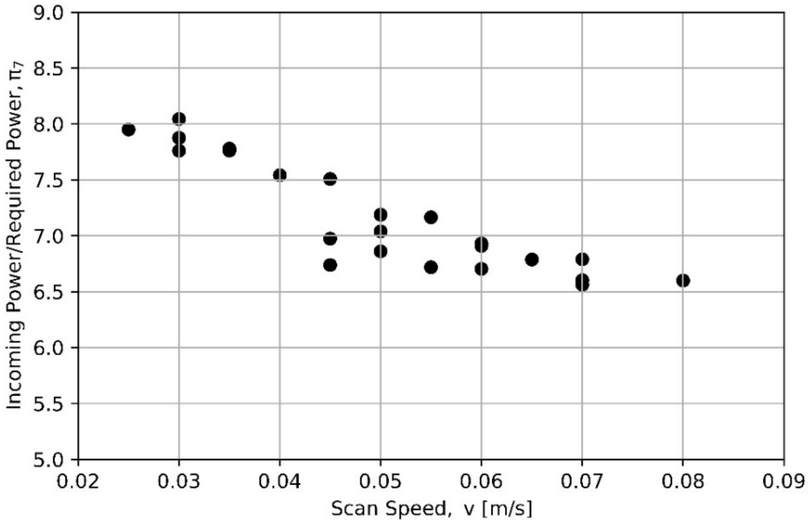

Figure 5.12: Power Ratio vs Scanning Velocity

Although there is seemingly a large variance between the points, the mean of this dataset is 7.2 while the variance is 0.24. This is very close to the mean value of the dimensionless number obtained during tests with powdered salts, confirming that this parameter is independent of material properties, barring absorptivity. This value again indicates that the amount of incoming radiation needed to cause sintering is vastly greater than the actual energy required. As with the salts, no attempt was made to model the conductive or convective losses for this parameter. Furthermore, the parameter only accounts for latent heat effects. Sensible heat effects— which amount to more per unit mass than latent— will further decrease the melting efficiency. However, the efficiencies obtained are within the bounds achievable with lasers when compared to the absorptivities obtained by Kruth et al. (2003).

A distinction can be made between the points where only sintering occurred and those where both sintering and melting occurred. This was done using the aforementioned microscope images at 5x magnification. Separating those that only sintered from those in which both melting and sintering occurs produces Figure 5.13.

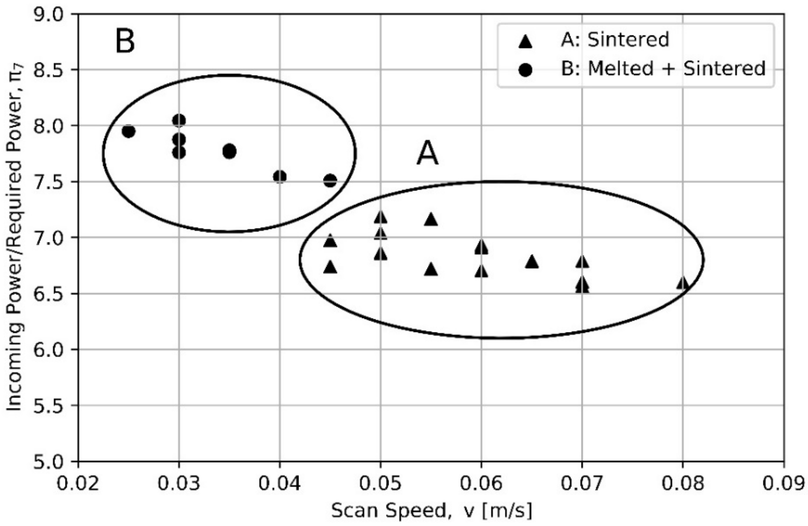

Figure 5.13: Power Ratio vs Scanning Velocity, Distinction between Sintered and Melted

A distinction between the two phenomena is clearly visible. The samples in which only sintering occurred consistently have a lower ratio of incoming power to required power. This can be easily explained: during sintering, only the outer layer of each particle undergoes melting, causing the required power to sinter a layer to be significantly less than if a layer of the same thickness were to be produced via melting. Additionally, a sintered layer cannot reach the same level of compaction as a molten layer. This is unaccounted for by the model which does not consider the porosity of the final product.

The mean of the sintered samples is 6.84 while the variance is decreased to 0.04. The smaller variance further validates the dimensional analysis.

A different way of portraying the data is through the realisation that the layer thickness is proportional to the ratio of incoming power to scanning velocity, as shown in Equation 3.19. Plotting this one obtains Figure 5.14.

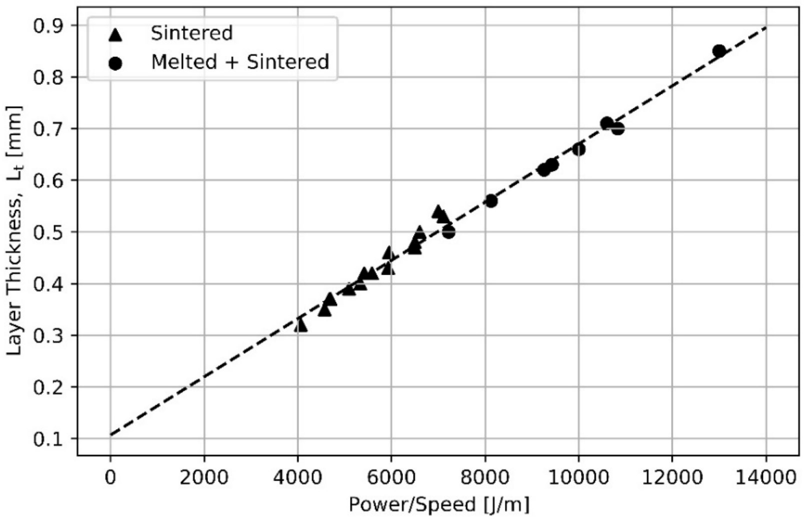

Figure 5.14: Power to Speed Ratio vs Layer Thickness

The proportionality is clearly confirmed by this graph. Noticeable, however, is that the projected line does not run through the origin. This is, at first, an unexpected result, as, at either no incident radiation or infinite scanning velocities, no sintering should occur. Rather, an intercept with the x-axis is expected as at low ratios of power to speed the incident radiation will cause a significant enough increase in sensible energy to induce melting. However, since this model also does not account for sensible energy changes or heat losses, this too can be explained. The projected intersection implies that, over the current range, the combined effects of heat losses and sensible energy changes are such that a layer thickness of 10^{-4} m could be created if these losses were not present. In reality, this graph is expected to taper off and approach zero as the ratio of power to speed approaches zero; however, at power to speed ratios lower than 4 000 J·m^{-1} the structural integrity of the sample is compromised. Similarly, the trend is not expected to be valid for regions significantly higher than those observed as thermal decomposition of the polymer will start to affect the process. Thermal decomposition of the polymer was noted to begin having a significant effect at power to speed ratios of around 16 000 J·m^{-1}. This value is expected to be a function of the thermal properties of the sample material as it is indicative of the fact that the rate of energy input, compared to its ability to conduct heat, is too great per unit volume of material. The material is not able to conduct enough heat away from the surface to prevent the temperature from reaching a critical value. For materials with a higher thermal diffusivity the range over which the current trend is valid would be larger.

5.3.4. Heat Transfer Model

Table 5.4 summarises the values used for the evaluation of the heat transfer model, resulting from the various models described in Chapter 3. The pure component property data for both Nylon and air were obtained from Çengel and Ghajar (2014: 917, 924).

Table 5.4: Heat Transfer Model Parameters

Parameter	Value
d	$3\ mm$
ρ	$1150\ \frac{kg}{m^3}$
C_P	$1700\ \frac{kJ}{kg\ K}$
λ	$96.7\ \frac{kJ}{kg}$
h	$12.48\ \frac{W}{m^2K}$

This spot size is, of course, significantly larger than what is achievable with a laser, lowering the heat flux and thereby increasing print time and decreasing the resolution of the printer. These factors limit the performance of the printer.

The calculated heat transfer coefficient seems plausible and was used in the present work to make predictions; however, the heat flux lost via natural convection is several orders of magnitude lower than the received heat flux due to radiation. It can therefore be safely ignored in practise.

Using these parameters one can plot the calculated layer thickness— calculated using Equation 3.19— against the measured layer thickness to investigate the accuracy of the model. This results in Figure 5.15.

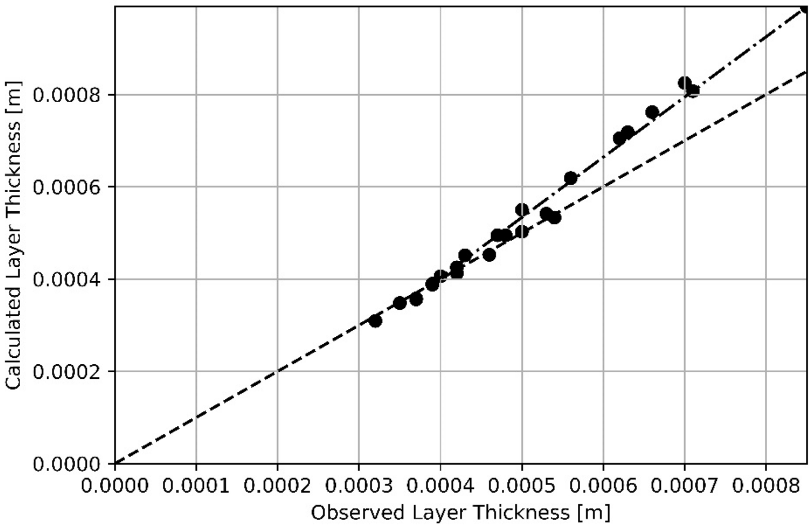

Figure 5.15: Observed vs Calculated Layer Thickness

Two distinct lines, as indicated in Figure 5.15, are clearly visible. It is to be expected that these two lines demonstrate the occurrence of two separate phenomena. The same distinction between sintered and melted samples, as made before, can now be used to produce Figure 5.16.

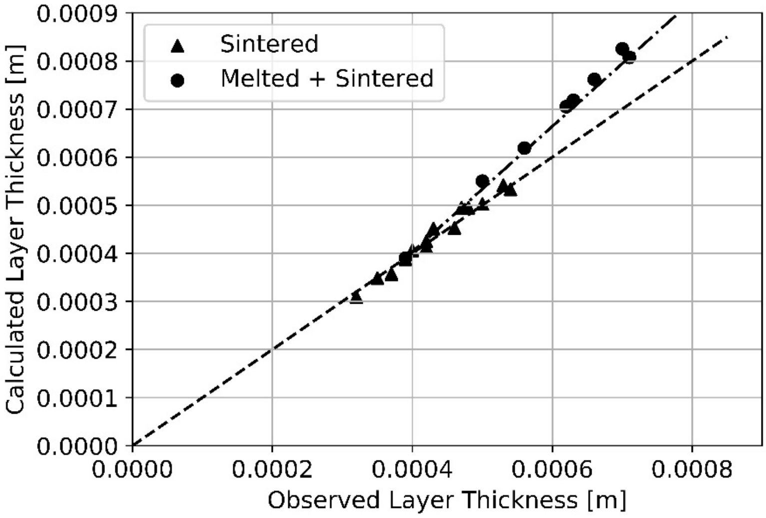

Figure 5.16: Observed vs Calculated Layer Thickness, Distinction between Sintered and Melted

The tuning parameter for this case was set at 0.67, indicating that the combined losses from reflection on the surface of the sample powder and conductive losses from the bottom of the bed amounted to 33 %. The RMS error of the predicted values compared to the samples that sintered is 2.74 %, indicating that the model fits the data well. After the tuning parameter had been fixed and the model verified, the model could be tested over a range of possible environments to see whether it meets constraints such as an infinitely thin layer thickness at infinitely low irradiances or infinitely high scan velocities. Because only the scan velocity can truly be varied during tests it was chosen to simulate over the diverse environments using 200 random combinations of incident irradiance and scanning speed— both parameters with values within reasonable ranges— and superimpose the measured data set. The result is Figure 5.17.

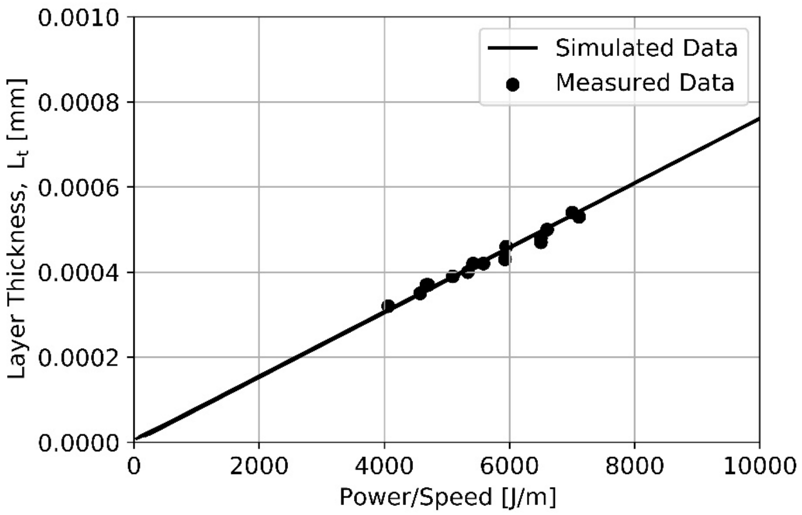

Figure 5.17: Simulated and Measured Layer Thickness

Clearly here, in comparison to earlier methods— such as the dimensional analysis that resulted in Figure 5.14— a much more reasonable result is obtained. The significant offset on the y-axis intercept is not present anymore, satisfying the boundary conditions stipulated earlier. Broadening of the line at lower values of the power to speed ratio is indicative of some model uncertainty as the model is not entirely linear and the heat transfer coefficient is piecewise continuous. In comparison to the variance between predicted and measured values this uncertainty is relatively small and can therefore safely be neglected.

5.4. Process Control

The most precise method of implementing the process control scheme would be to adjust the velocity of the motors as close to continuously as possible. With stepper motors this implies changing the velocity on a ‘per step’ basis. However, because the velocity has to be calculated in between steps, with the stepper motor ‘idle’ during this short period, implementing velocity changes this often would result in significant vibrations. These would not only have a detrimental effect on the quality of a print, but, over prolonged periods, also on the mechanical integrity of the printer. It was therefore decided to implement velocity on a ‘per track’ basis. The track sizing used in testing was 10 cm. The maximum track sizing allowed for by the platform is approximately 20 cm. On average, during the testing phase, scanning along a single track took ~ 2 s. It is unlikely that the incident radiation would fluctuate significantly during this time. To confirm this the relative difference of the incident radiation from the mean for each track over multiple runs is shown in Figure 5.18 below. The runs were, on average, 2 minutes long.

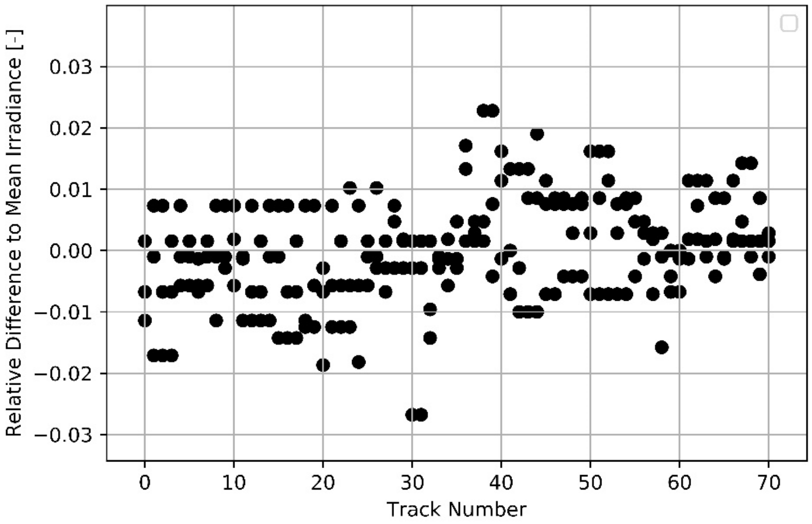

Figure 5.18: Relative Difference of Incident Radiation from Mean at Mid-day

The mean solar irradiation observed over all runs was 348.9 W·m^{-2}, while the average standard deviation from the mean of each particular run was 3.5 W·m^{-2}. This confirms that a control system implementing changes on a 'per track' basis is sufficient.

Through implementation of the control scheme, reasonable control over the sintering depth was achievable, as is illustrated by Figure 5.19.

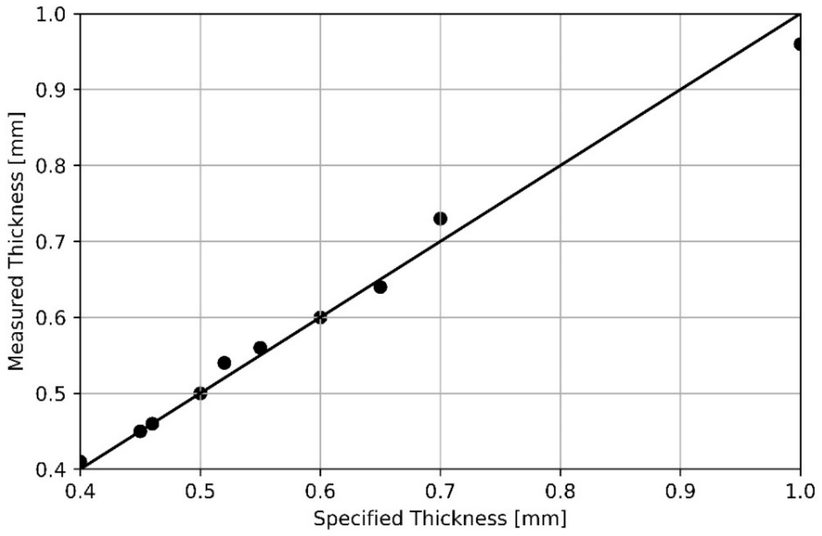

Figure 5.19: Specified vs Measured Thickness

The RMS error for this dataset is 2.44 %. This was deemed low enough for the control scheme to be implemented for 3D tests. The fluctuation of data points with values both higher and lower than specified values could be due to the process control scheme adjusting values every track, as opposed to instantaneously, allowing for natural fluctuations in incident radiation to have a greater effect. A more serious error would be incorrect model equations.

5.5. Applicability

The extent to which a device such as this can be implemented depends drastically on the amount of sunlight received in the region it is to be implemented in. To quantify the degree with which a device such as this can be implemented, a comparison of the number of hours that the DNI at a region exceeds a threshold value can be made. Although a lower limit of 4 000 J·m^{-1} for the Power to Speed ratio has been stated previously, the printer required incoming solar radiation of at least 280 W·m^{-2} to function properly. Factoring in the losses incurred over the two mirrors results in a required DNI of at least 608 W·m^{-2}. To ensure continuous operation, a minimum DNI threshold of 650 W·m^{-2} is therefore imposed. Table 5.5 summarises the applicability of this technology in six major South African cities for the year 2016 using data provided by the South African Universities Radiometric Network (Brooks et al., 2015). As the DNI threshold is usually exceeded during working hours, a fractional utilisation is given as the ratio of hours where the threshold is exceeded to average number of working hours, based on an eight-hour working day.

Table 5.5: Varying Applicability of Developed Technology in South African Cities

City	Province	Annual DNI threshold exceeding hours	Fractional Utilisation
Richtersveld	Northern Cape	2717	0.93
Bloemfontein	Free State	2290	0.78
Stellenbosch	Western Cape	2155	0.74
Pretoria	Gauteng	1899	0.65
Port Elizabeth	Eastern Cape	1208	0.41
Durban	Kwa-Zulu Natal	1134	0.39

This is the expected result (compare Figure 2.3). The average DNI is highest in the Northern Cape and declines steadily to a low average DNI at South Africa's eastern coasts. Clearly, while highly applicable in areas such as the Northern Cape, it is not recommended to be utilised in the eastern coastal areas. The utilisation could be markedly improved by reducing losses over the mirrors. If the losses over the mirrors could be limited to 20 % less than currently, the utilisation would increase by 15 % in Durban while allowing near constant usage throughout the working day in the Northern Cape and Free State. While hourly DNI data is not available for other regions, based on Figure 2.2 one could expect similar utilisation in the southern parts of Europe as in Durban, while heavy utilisation is possible in the southern states of the USA, Australia, the Middle-East and eastern parts of South America.

6. Conclusion and Recommendations

A 3D printer, using only concentrated solar power to sinter a powdered material has been successfully constructed and tested. In order to calibrate the printer a mixture of powdered salts has been used. This mixture has a few advantages over conventional SLS powders as a model material, such as its inert behaviour in an oxidising atmosphere and its quick crystallisation, preventing warping.

In order to select the correct mixture of salts a thermodynamic model has been developed from first principles. This model has the capabilities of predicting both temperature-composition and latent heat of fusion-composition. To determine the validity of the model it has been compared to the data of 21 eutectic salt mixtures found in literature. Temperature-composition was calculated using the Schröder-van Laar equation. This equation was able to predict the eutectic temperature reasonably accurately, displaying an RMS error of only 12 %. Its ability to predict the eutectic composition is slightly worse, at an error of 25.5 %. The entropic approach, developed to model latent heat of fusion-composition, initially showed a large deviation from latent heat of fusion-composition data obtained from literature. This was found to be due to an excessive contribution from the enthalpy of mixing. Omitting this term produced significantly better results, the new method being classified as a 'modified entropic approach'. This approach was able to calculate latent heat of fusion-composition, with an RMS error of 24.7 %, using only the latent heat of fusion and melting temperature of the pure components. Using a correlation known as "Richard's Rule" it has been confirmed that this method can be adapted to use only pure component melting point data to model latent heat of fusion-composition data. This adaptation decreases the accuracy of the model to an RMS error of 30.6 %. Using this approach, the $NaNO_3$-KNO_3 system has been determined to be a valid model system to represent Nylon SLS polymer powders. This has been confirmed through literature data of the system.

The constructed solar 3D printer has been analysed, through use of a dimensional analysis, and tested with the $NaNO_3$-KNO_3 salt system. To increase the absorptivity to solar radiation, carbon black was dry-mixed into the salt mixture. A low melting efficiency was observed as indicated by the high ratio of incoming power to power required to induce sintering. This ratio was found to have a low variance, validating the dimensional analysis. Because of the successful tests on powdered salts, tests were conducted on commercial SLS powder next. These displayed very similar results to the salt tests, indicating that the parameter is not limited to a certain material, provided that the different materials show similar absorption characteristics. Degradation of the polymer material was noted to begin occurring at 16 000 $J{\cdot}m^{-1}$. Using these results, a comprehensive model was used to compare predicted values to measured values of the sintered depth. Two trends were observed. These were found to correspond to those values that had only undergone sintering and those that had undergone both sintering and melting respectively. The predicted values differed only by 2.74 % to the predicted values after having tuned the model to compensate for reflective and conductive losses. Using this information, a process control scheme, based on the model, equations was developed. It was found that adjusting printing speed after every track is sufficient and does not cause unnecessary stress on the printer. The control scheme was able to sinter to the specified depth with only an error of 2.4 %. A concern for the printer is the large spot size, drastically limiting the achievable resolution and heat flux. Although high concentration ratios were observed they are far from ideal. Significant improvement is necessary for this technology to be within the realm of conventional SLS in this regard.

To further this work, it is recommended to test varieties of concentration methods to increase the achievable resolution. If necessary, filtering out unwanted radiation, which would decrease the spot size without increasing the heat flux, can be considered. Furthermore, tests should be conducted to develop a system— or modify an existing system— capable of depositing powdered material in layers. Preliminary work has shown this system is capable of sintering multiple layers; however, significant improvement is necessary for this to be achievable in a controlled fashion. Tests on materials already used in SLS, such as Titanium, should also be considered. To conduct preliminary tests a eutectic mixture of KF-LiCl can be used, due to its similar latent heat of fusion. Research can also be conducted into the implementation of a control system that can infer the position of the collimating mirror from the time of day and global position. This will eliminate both drift or sudden changes of the focal point.

7. References

Agarwala, M., Bourell, D., Beaman, J., Marcus, H., & Barlow, J. (1995). Direct selective laser sintering of metals. *Rapid Prototyping Journal*, *1*(1), 26–36.

Badenhorst, H., & Böhmer, T. (2018). Enthalpy of fusion prediction for the economic optimisation of salt based latent heat thermal energy stores. *Journal of Energy Storage*, *20*(December), 459–472. https://doi.org/10.1016/j.est.2018.10.020

Badenhorst, H., Fox, N., & Mutalib, A. (2016). The use of graphite foams for simultaneous collection and storage of concentrated solar energy. *Carbon*, *99*, 17–25. https://doi.org/10.1016/j.carbon.2015.11.071

Bertrand, P., Bayle, F., Combe, C., Goeuriot, P., & Smurov, I. (2007). Ceramic components manufacturing by selective laser sintering. *Applied Surface Science*, *254*(4), 989–992. https://doi.org/10.1016/j.apsusc.2007.08.085

Brand, L. (1957). The Pi Theorem of Dimensional Analysis. *Archive for Rational Mechanics and Analysis*, *1*(1), 35–45.

Brooks, M. J., du Clou, S., van Niekerk, W. L., Gauche, P., Leonard, C., Mouzouris, M. J., … Vorster, F. J. (2015). SAURAN : A new resource for solar radiometric data in Southern Africa. *Journal of Energy in South Africa*, *26*(1), 2–10.

Bugeda, M., Cervera, G., & Lombera, G. (1999). Numerical prediction of temperature and density distributions in selective laser sintering processes. *Rapid Prototyping Journal*, *5*(1), 21–26.

Çengel, Y. A., & Ghajar, A. J. (2014). *Heat and Mass Transfer: Fundamentals & Applications*. McGraw-Hill Education. Retrieved from https://books.google.co.za/books?id=1YPhoAEACAAJ

Childs, T. H. C., Berzins, M., Ryder, G. R., & Tontowi, A. (1999). Selective laser sintering of an amorphous polymer—simulations and experiments. *Proceedings of the Institution of Mechanical Engineers, Part B: Journal of Engineering Manufacture*, *213*(4), 333–349. https://doi.org/10.1243/0954405991516822

Craig, O. O., Brent, A. C., & Dinter, F. (2017). The current and future energy economics of concentrating solar power (CSP) in south africa. *South African Journal of Industrial Engineering*, *28*(3), 1–14.

Dong, L., Makradi, A., Ahzi, S., & Remond, Y. (2009). Three-dimensional transient finite element analysis of the selective laser sintering process. *Journal of Materials Processing Technology*, *209*(2), 700–706. https://doi.org/10.1016/j.jmatprotec.2008.02.040

Fischer, P., Locher, M., Romano, V., Weber, H. P., Kolossov, S., & Glardon, R. (2004). Temperature measurements during selective laser sintering of titanium powder. *International Journal of Machine Tools and Manufacture*, *44*(12–13), 1293–1296. https://doi.org/10.1016/j.ijmachtools.2004.04.019

Fluri, T. P. (2009). The potential of concentrating solar power in South Africa. *Energy Policy*, *37*(12), 5075–5080. https://doi.org/10.1016/j.enpol.2009.07.017

Gusarov, A. V., Laoui, T., Froyen, L., & Titov, V. I. (2003). Contact thermal conductivity of a powder bed in selective laser sintering. *International Journal of Heat and Mass Transfer*, *46*(6), 1103–1109. https://doi.org/10.1016/S0017-9310(02)00370-8

Gusarov, A. V., Yadroitsev, I., Bertrand, P., & Smurov, I. (2007). Heat transfer modelling and stability analysis of selective laser melting. *Applied Surface Science*, *254*(4), 975–979. https://doi.org/10.1016/j.apsusc.2007.08.074

Huang, S. H., Liu, P., Mokasdar, A., & Hou, L. (2013). Additive manufacturing and its societal impact: A literature review. *International Journal of Advanced Manufacturing Technology*, *67*(5–8), 1191–1203. https://doi.org/10.1007/s00170-012-4558-5

Kenisarin, M. M. (2010). High-temperature phase change materials for thermal energy storage. *Renewable and Sustainable Energy Reviews*, *14*(3), 955–970. https://doi.org/10.1016/j.rser.2009.11.011

Kleppa, O. (1960). A New Twin High-Temperature Reaction Calorimeter. The Heats of Mixing in Liquid Sodium-Potassium Nitrates. *The Journal of Physical Chemistry*, *64(12)*, 1937–1940.

Kosa, L., Proks, I., Strečko, J., Adamkovičová, K., & Nerád, I. (1993). Estimation of the heat of fusion of binary compounds and of eutectic using thermodynamic balances. *Thermochimica Acta*, *230*(C), 103–111. https://doi.org/10.1016/0040-6031(93)80351-A

Kruth, J. P., Wang, X., Laoui, T., & Froyen, L. (2003). Lasers and materials in selective laser sintering. *Assembly Automation*, *23*(4), 357–371.

Kumar, V., Shrivastava, R. L., & Untawale, S. P. (2015). Fresnel lens: A promising alternative of reflectors in concentrated solar power. *Renewable and Sustainable Energy Reviews*, *44*, 376–390. https://doi.org/10.1016/j.rser.2014.12.006

Leutz, R., & Suzuki, A. (2012). *Nonimaging Fresnel lenses: design and performance of solar concentrators* (Vol. 83). Springer.

Levy, G. N., Schindel, R., & Kruth, J. P. (2003). Rapid Manufacturing and Rapid Tooling With Layer Manufacturing (Lm) Technologies, State of the Art and Future Perspectives. *CIRP Annals*, *52*(2), 589–609. https://doi.org/10.1016/S0007-8506(07)60206-6

Osswald, T. A. (2015). *Understanding Polymer Processing: Processes and Governing Equations*. Carl Hanser Verlag GmbH & Company KG.

Prince, J. D. (2014). 3D Printing: An Industrial Revolution. *Journal of Electronic Resources in Medical Libraries*, *11*(1), 39–45. https://doi.org/10.1080/15424065.2014.877247

Richards, J. (1897). Relations Between the Melting Points and the Latent Heats of Fusion of the Metals. *Journal of the Franklin Institute*, *143*(5), 379–383.

Rietma, M. J. (2012). *Design of a Solar Sand Printer*. University of Twente.

Seborg, D. E., Mellichamp, D. a., Edgar, T. F., Doyle, F. J., & Iii. (2004). Process Dynamics and Control. Retrieved from http://books.google.pt/books/about/Process_Dynamics_and_Control.html?id=_PQ42kOvtfwC&pgis=1

Sierra, C., & Vazquez, A. J. (2005). High solar energy concentration with a Fresnel lens. *Journal of Materials Science*, *40*, 1339–1343. https://doi.org/10.1007/s10853-005-0562-6

Simchi, A. (2006). Direct laser sintering of metal powders: Mechanism, kinetics and microstructural features. *Materials Science and Engineering A*, *428*(1–2), 148–158. https://doi.org/10.1016/j.msea.2006.04.117

Smith, J. M., Van Ness, H. C., & Abbott, M. M. (2005). *Introduction to chemical engineering thermodynamics*. McGraw-Hill Education.

Tolochko, N. K., Arshinov, M. K., Gusarov, A. V., Titov, V. I., Laoui, T., & Froyen, L. (2003). Mechanisms of selective laser sintering and heat transfer in Ti powder. *Rapid Prototyping Journal*, *9*(5), 314–326. https://doi.org/10.1108/13552540310502211

Van Elsen, M., Al-Bender, F., & Kruth, J. P. (2008). Application of dimensional analysis to selective laser melting. *Rapid Prototyping Journal*, *14*(1), 15–22. https://doi.org/10.1108/13552540810841526

Vasquez, M., Haworth, B., & Hopkinson, N. (2011). Optimum sintering region for laser sintered Nylon-12. *Proceedings of the Institution of Mechanical Engineers, Part B: Journal of Engineering Manufacture*, *225*(12), 2240–2248. https://doi.org/10.1177/0954405411414994

Walas, S. M. (2013). *Phase equilibria in chemical engineering*. Butterworth-Heinemann.

Walden, P. (1908). Uber die Scmelzwarme, Spezifische Kohasion und Molekulargrosse bei der Schmelztemeratur. *Zeitschrift Fur Elektrochemie*, (43).

Wang, X. C., Laoui, T., Bonse, J., Kruth, J. P., Lauwers, B., & Froyen, L. (2002). Direct Selective Laser Sintering of Hard Metal Powders : Experimental Study and Simulation. *International Journal of Advanced Manufacturing Technology*, *19*, 351–357.

Welty, J., Rorrer, G. L., & Foster, D. G. (2014). *Fundamentals of Momentum, Heat, and Mass Transfer, Revised 6th Edition*. Wiley.

Williams, J. D., & Deckard, C. R. (1998). Advances in modeling the effects of selected parameters on the SLS process. *Rapid Prototyping Journal*, *4*(2), 90–100.

Xie, W. T., Dai, Y. J., Wang, R. Z., & Sumathy, K. (2011). Concentrated solar energy applications using Fresnel lenses: A review. *Renewable and Sustainable Energy Reviews*, *15*(6), 2588–2606. https://doi.org/10.1016/j.rser.2011.03.031

Yagi, S., & Kunii, D. (1957). Studies on effective thermal conductivities in packed beds. *AIChE Journal*, *3*(3), 373–381.

Yap, C. Y., Chua, C. K., Dong, Z. L., Liu, Z. H., Zhang, D. Q., Loh, L. E., & Sing, S. L. (2015). Review of selective laser melting: Materials and applications. *Applied Physics Reviews*, *2*(4). https://doi.org/10.1063/1.4935926

Zeng, K., Pal, D., & Stucker, B. (2012). A review of thermal analysis methods in Laser Sintering and Selective Laser Melting Kai Zeng, Deepankar Pal, Brent Stucker Department of Industrial Engineering, University of Louisville, Louisville, KY 40292. *Solid Freeform Fabrication Symposium*, 796–814.

Zhang, Y., & Faghri, A. (1999). Melting of a subcooled mixed powder bed with constant heat flux heating. *International Journal of Heat and Mass Transfer*, *42*(5), 775–788. https://doi.org/10.1016/S0017-9310(98)00231-2